From bulk to molecularly thin hybrid perovskites

Kai Leng[1,2], *Wei Fu*[1,2], *Yanpeng Liu*[1,2], *Manish Chhowalla*[3] *and Kian Ping Loh*[1,2] ✉

Abstract | Organic–inorganic hybrid perovskites have been intensively researched in the past decade for their optoelectronic properties. The emergence of Ruddlesden–Popper perovskites, which have mixed dimensionality, has heralded new opportunities for tailor-made semiconductors that combine enhanced stability with useful properties between those of 2D and 3D systems. Inspired by advances in 2D materials research, there is growing interest in molecularly thin versions of these hybrid perovskites, owing to their ease of incorporation into electronic devices. There is, thus, a need to understand thickness-dependent electrical, excitonic and phononic properties that go beyond quantum-confinement effects. Recent studies have shown that, apart from tuning the dimensionality of the system, fine-tuning its thickness also helps to optimize performance in different applications, ranging from third-harmonic generation to photodetectors and spintronics.

The past decade has witnessed an explosion of research in organic–inorganic hybrid perovskites, due to their unique excitonic properties and remarkable performance in photovoltaics and optoelectronic devices[1–8]. Beyond 3D hybrid perovskites, layered Ruddlesden–Popper perovskites (RPPs) have emerged as more environmentally stable alternatives that exhibit dielectric and quantum-confinement effects. RPPs are an archetypical class of dimensionality-controlled layered compounds described by the formula $((RNH_3)_2(CH_3NH_3)_{n-1}A_nX_{3n+1})$, where R is an alkyl or aromatic moiety, A a metal cation, X a halide and n the number of inorganic metal-halide-perovskite layers[9–11]. RPPs consist of inorganic layers of metal-halide perovskites confined by wide-bandgap and low-dielectric-constant organic cations. Such a structural arrangement is akin to bandgap confinement in quantum wells[12–15], that is, the semiconducting inorganic halide atomic layers are electronically isolated by the insulating organic chains, leading to large exciton-binding energies, high oscillator strengths, short exciton-decay times and reduced effective exciton radii[8,16–20]. The organic chains in RPPs are responsible for dielectric confinement and for the materials' hydrophobicity, stability[21,22], structural rigidity[23,24] and tuneable sheet-to-sheet distance[25–27]. By engineering the compositions of the organic moieties, RPPs can be obtained as quasi-2D ($1 < n < \infty$) or 2D ($n = 1$) crystals (FIG. 1a). Increasing the value of n results in an increased thickness of the unit cell and in a reduction of the bandgap and excitonic-binding energies. Tuning the value of n (that is, the dimensionality) has been used as a strategy to enhance the energy and charge transfer in photovoltaic devices[28–34].

In order to incorporate 2D RPP crystals into electronic devices, controlling the thickness as well as the lateral size of the crystal is essential. The relatively weak interactions between the organic chains of two unit cells enable mechanical exfoliation of thin flakes using the techniques developed for graphene and other 2D materials[35–40]. Generally, flakes with thickness larger than 100 nm have properties similar to those of the bulk crystal. Thin flakes, with thicknesses in the 20–60 nm range, have the optimal thickness for non-linear optical (NLO) effects, such as third-harmonic generation (THG), which manifest strongly. Crossover to the 2D regime occurs at a thickness below 10 nm, which is achieved by the isolation of a single or double RPP unit cell. Given that 2D RPPs are molecularly soft due to weak ionic and hydrogen bonds[41–43], in these systems, a much bigger lattice deformation than in bulk crystals is expected in response to strain, electric fields and light or thermal activation. In addition, surface and interface effects assume a more dominant role in such molecularly thin crystals, strongly influencing energy and charge-transfer effects[44,45]. For example, in molecularly thin RPPs, surface-inversion symmetry is likely to be broken, owing to surface disorder or lattice reconstructions; this may result in a surface potential that penetrates the whole volume of the ultra-thin crystal, leading to Rashba-band splitting. More research is needed to understand how the exciton-binding energy, dielectric constant and spatial extension of the electron and hole wave functions change as thickness crosses over to the 2D regime. Substrate interactions can strongly influence electron–hole Coulomb interactions in molecularly thin layers; thus, the choice of support requires careful consideration[46]. The isolation of large molecularly thin single

[1]*Department of Chemistry, National University of Singapore, Singapore, Singapore.*

[2]*Centre for Advanced 2D Materials and Graphene Research Centre, Singapore, Singapore.*

[3]*Department of Materials Science and Metallurgy, University of Cambridge, Cambridge, UK.*

✉*e-mail: chmlohkp@nus.edu.sg*

https://doi.org/10.1038/s41578-020-0185-1

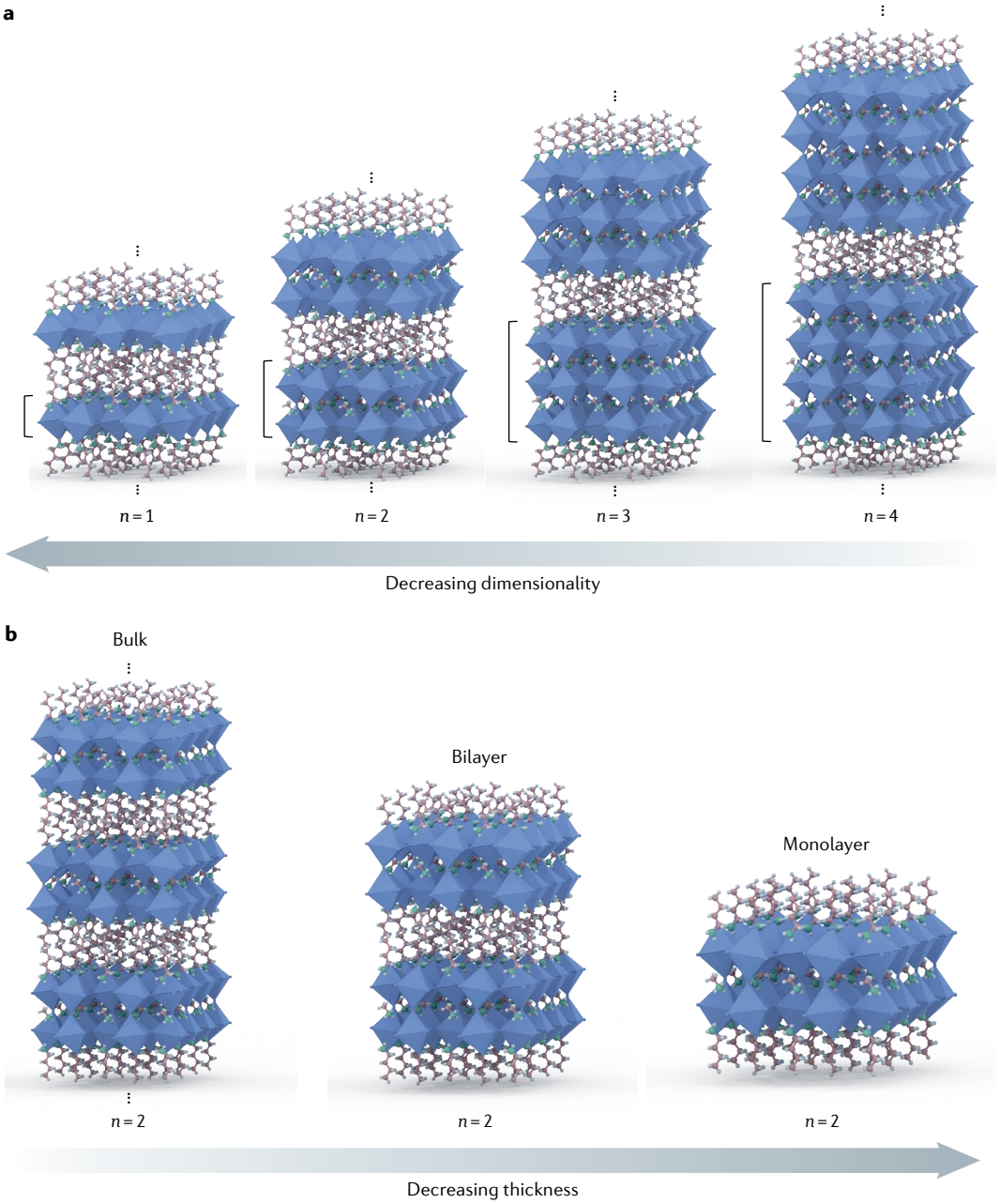

Fig. 1 | **Decreasing dimensionality and thickness in hybrid 2D perovskites. a** | Crystal structures of Ruddlesden–Popper hybrid 2D perovskites, $(BA)_2(MA)_{n-1}Pb_nI_{3n+1}$ (number of inorganic layers $n = 1$–4), illustrating the structural transition from $n = 4$ to $n = 1$. **b** | Thickness reduction in 2D perovskites (taking $(BA)_2(MA)Pb_2I_7$; $n = 2$ as an example). The bulk crystal contains infinite inorganic quantum wells, whereas the monolayer crystal contains only one.

crystals without grain boundaries is especially useful for investigating how the intrinsic photophysical and electronic properties in these systems deviate from those of the bulk[47,48].

In this Review, we describe how the physical properties of RPPs evolve as a function of thickness going from bulk to molecularly thin 2D perovskites[49]. Specifically, we review recent work in which thickness and dimensionality have been employed to control the properties of 2D perovskites, and we discuss how phase-pure RPPs with $n > 1$ present a unique opportunity to explore the physical properties of semiconducting crystals with mixed dimensionality, between that of monolayer 2D perovskites and of 3D perovskites. Understanding how the quasi-2D physics of these materials is modulated by compositional and dimensional engineering helps to optimize device performance. We also survey the synthesis methods, photophysical properties and device demonstrations for both quasi-2D and truly 2D hybrid-perovskite materials.

Structure and dimensionality

Structure. The spatial arrangement of the organic and inorganic components is used to classify the dimensionality of hybrid perovskites. In 3D perovskites, the structure consists of a 3D network of corner-sharing

$[MX_6]^{4-}$ octahedra. In 2D perovskites, large aliphatic or aromatic organic cations (such as *n*-butylammonium (*n*-BA) or 2-phenylethylammonium (PEA)) act as spacers to partition the cubic 3D framework into well-defined 2D slabs. When the number of inorganic perovskite layers is reduced from $n = \infty$ to $n = 1$, the system changes from 3D to 2D. Similarly, when *n* goes from 4 to 1, a dimensional transition from quasi-2D to fully 2D is observed (FIG. 1a). Decreasing the thickness of layered perovskite-bulk crystals leads to a transition from a finite number of electronically isolated quantum wells to a single quantum well surrounded by organic chains (FIG. 1b). Taking $n = 2$ RPPs as an example, the unit cell is defined by two layers of inorganic quantum wells that are separated by two rows of partially interlocked *n*-BA organic chains. The weakest link in the structure is the van der Waals force between the partially interlocked *n*-BA organic chains. Under pressure, interlayer sliding can occur, owing to a shift in interdigitation of the interlocked organic chains or to shear deformation of the flexible chains under mechanical force[50,51]. The inorganic halide layers, held together by in-plane ionic bonds, have a higher resistance to plastic deformation than the organic chains[52–54], which are held together by interchain van der Waals forces and anchored by both electrostatic bonds between the positively charged ammonium moieties and the negatively charged halide ions[55]. Therefore, by increasing the space occupied by the organic moieties, for example, by increasing chain lengths from $-C_4H_9$ to $-C_{12}H_{25}$, the Young's modulus decreases to a saturation threshold determined by the bonding in the inorganic moieties[56].

Mechanics. Based on nanoindentation studies on 2D RPP crystals, the out-of-plane Young's modulus (~3.3 GPa), which is limited by the van der Waals forces of the organic chains, is at least one order of magnitude lower than that measured for hexagonal boron nitride, h-BN (24.5–27 GPa)[57,58], highly oriented pyrolytic graphite (36.5 GPa)[59,60] and MoS_2 (52 GPa)[61]. The smaller overall elastic modulus of layered perovskites explains why they are easier to exfoliate than graphite and transition-metal dichalcogenides. As the weakest link is constituted by the interlayer binding forces between the organic chains, engineering the packing of the chains influences the exfoliation process. For example, using chains with PEA allows stronger π–π stacking, making exfoliation more difficult than in a structure containing the *n*-BA cation[62–64].

Deformation. After exfoliation, organic chains remain at the top and bottom of the inorganic layer (FIG. 1b). These organic chains are held together principally by hydrogen bonding between the ammonium moieties of the organic chain and the halogens of the anionic cage. In the absence of steric hindrance caused by the interlocked bilayer, the remaining organic chains can be readily disoriented by laser illumination and mechanical stress, leading to local disorder of the organic cations and deformation of the inorganic framework[40]. In particular, molecularly thin 2D RPP layers may show photostriction or electrostriction, effects related to changes in the internal strain and, therefore, shape, upon the application of light or of an electric field[65,66]. Whereas piezoelectricity is a first-order effect, owing to the linear relationship between strain and electric field, electrostriction is a second-order effect, with the electromechanical strain proportional to the square of the electric field. Thus, electrostriction is distinguishable from the inverse piezoelectric effect, and a centrosymmetric crystal can exhibit electrostriction without being piezoelectric. A giant photostriction coefficient of 1.25% has been reported for $MAPbBr_3$ (MA: CH_3NH_3), in which the strain in the crystal was monitored by Raman spectroscopy upon laser irradiation[65]. In 3D perovskites, photostriction has been rationalized as the weakening of the hydrogen bonding between the organic cations and the inorganic lattice by photo-generated carriers, and has been proposed to be important for understanding optical effects[66].

Such optomechanical or electromechanical coupling in perovskites can form the basis of fast and highly sensitive mechano-optical or electro-optical actuator devices. For example, $MAPbI_3$ single crystals exhibit a compressive strain of up to 1% for a mechanical energy density of 0.74 J cm^{-3}, which is higher than that of most electrostrictive materials[67]. Compared with piezoelectric materials showing 0.1% strain, electrostrictive materials can achieve a strain of 5% or more. The deformation energy of hybrid organic–inorganic crystals decreases with thickness and dimensionality; thus, thin 2D RPP crystals are expected to exhibit strong photostriction and electrostriction. Owing to the form factor of ultra-thin 2D perovskites, they are highly suited for photostrictive or electrostrictive wearable devices, with a response potentially larger than that of traditional piezoelectric devices.

Making ultra-thin crystals

Depending on whether the source material is 2D or 3D perovskites, the methods to reduce their thickness to the ultra-thin limit differ. On account of their van der Waals stacked structure, mechanical exfoliation can be used to produce 2D RPPs with a thickness of a single quantum well; molecularly thin layers can also be produced by solution-phase or vapour-phase deposition methods. Owing to the non-layered structure of 3D perovskites, their thickness reduction has been achieved using precipitation, recrystallization and chemical-vapour-deposition methods[68–70].

Solution method. The first molecularly thin 2D hybrid perovskite (with mainly $n = 1$) was grown using the antisolvent method[71]. A ternary co-solvent of dimethylformamide, chlorobenzene and acetonitrile was used to adjust the solubility of the bulk perovskite. Then, the solution was drop-casted on a substrate and dried under mild heating to precipitate uniform square sheets (FIG. 2a). Although the drop-casting method is relatively simple, its disadvantages include flake aggregation, thickness inhomogeneity and the small size of the crystallites.

For 2D perovskites with $n = 1$, the Goldschmidt's tolerance factor, which is underpinned by steric constraints in 3D hybrid perovskites, is strongly relaxed, and

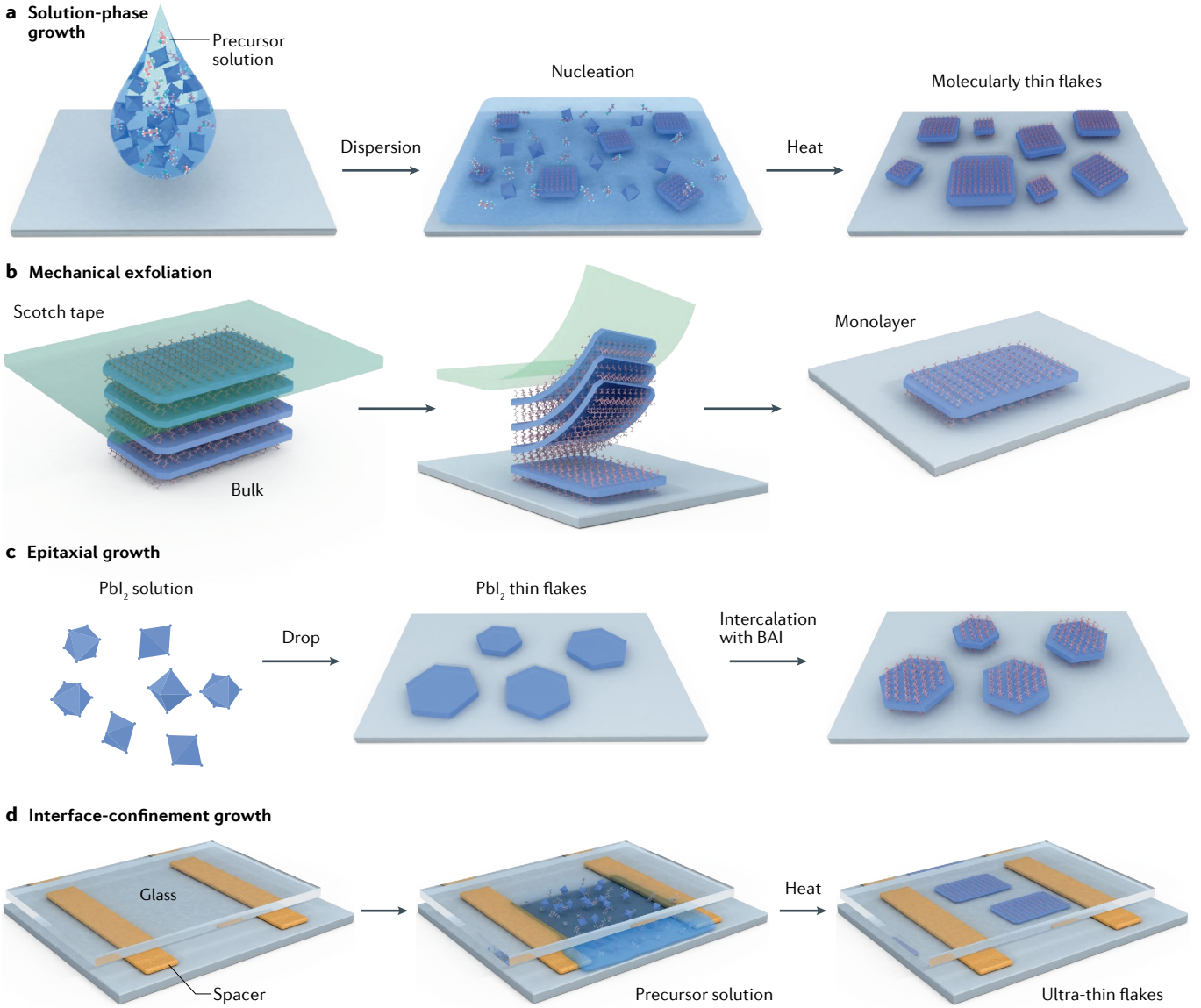

Fig. 2 | **Growth methods for thin 2D perovskite single crystals. a** | Solution-phase growth method. **b** | Mechanical-exfoliation method. **c** | Epitaxial-growth method. BAI, butylammonium iodide. **d** | Interface-confinement growth method.

much longer organic cations or larger inorganic anion cages can be used without phase segregation[72]. Thus, large organic cations such as phenylethylammonium ions ($C_8H_9NH_3^+$) (REF.[73]) and biimidazolium dications ($C_5H_{13}N_2^+$) (REF.[74]) can access the space between the inorganic layers. Recently, bulky and hydrophobic organic conjugated groups based on tetrathiophene ligands with monoammonium end groups were used to synthesize molecularly thin perovskite single crystals; the bulky ligands suppressed intermolecular self-aggregation and self-crystallization, facilitating the growth of crystals as thin as a single monolayer unit cell[75].

By careful compositional control, it is possible to generate RPPs with up to $n = 7$ for the $(BA)_2(MA)_{n-1}Pb_nI_{3n+1}$ series, the largest unit cell in a 2D perovskite with long-range crystallographic order known to date[76]. This provides a much larger compositional space to engineer new material properties. However, for RPPs with $n \geq 2$, there is a strong tendency towards phase segregation, disproportionation into mixed 3D and 2D phases, or occurrence of smaller n homologues. Therefore, the synthesis must be carefully controlled. To grow phase-pure RPP crystals with high n values, crystallization at an elevated temperature is required to allow the 2D RPPs to preferentially crystallize over PbI_2 in a concentrated HI reaction solvent[77]. In addition, careful control of the relative concentration of the precursors is important. When stoichiometric amounts of precursors are used, there is competition between the crystallization of 2D RPPs and 3D perovskites[9,40,78]. One synthesis strategy exploits the fact that the solubility of the RPP increases with n; thus, by lowering the temperature in a graded manner, it is possible to precipitate the least stable $n = 1$ crystals first, followed by the $n = 2$ crystals. If the $n = 1$ crystals are not separated from the solution, then the $n = 2$ crystals can nucleate on both their faces to form a ternary heterostructure; a narrow dual-band photodetector has been fabricated using this strategy[79].

Mechanical exfoliation. Similar to the mechanical-exfoliation method used for isolating graphene[80], bulk layered RPP crystals can be exfoliated by overcoming the weak van der Waals forces between the organic layers[81] (FIG. 2b). A temperature-programmed crystallization method has been developed to grow centimetre-scale RPPs ($n = 1, 2, 3, 4$), from which large (20–100 µm) molecularly thin layers can be exfoliated[40]. The surface of the exfoliated crystal is terminated by a layer of organic cations, as proved by the square symmetry of the surface atoms, which can be assigned to a well-ordered organic wire assembly, as discussed later in the context of the thickness-dependent optical properties of the material.

Not all layered perovskite crystals are suitable as source material for the isolation of molecularly thin layers. For example, exfoliating hybrid Dion–Jacobson 2D perovskites, in which the divalent (2^+) interlayer organic chains are linked by strong ionic bonds to the inorganic layers, is difficult[82]. 2D perovskites with alternating cations between the layers are also hard to exfoliate, owing to the presence of spacer cations such as guanidinium $(C(NH_2)_3)^+$ and methylammonium $(MA)^+$ (REF.[83]). A different strategy may be needed to obtain molecularly thin layers of these perovskites, perhaps via organic molecular-beam epitaxy or atomic-layer-engineering methods[84].

Epitaxial growth. A synthetic strategy combining solution synthesis and gas–solid-phase intercalation has been developed to grow 2D perovskite microplates with spatial precision and controlled thickness[85,86] (FIG. 2c). A similar method has also been reported for the synthesis of 3D perovskite microplates[87,88]. PbI_2 microplates were first grown on substrates either by directly dropping a saturated PbI_2 aqueous solution or via a pattern-growth method. The as-grown PbI_2 microplates were then placed downstream of a quartz tube to react with butylammonium iodide vapour evaporated from a source powder placed at the centre of the tube furnace. This way, hexagonal-phase PbI_2 was converted into an orthorhombic-phase 2D perovskite. A complete gas-phase synthesis should be possible if PbI_2 could be deposited from a gaseous source. As a step in this direction, an atomic-layer-deposition process for PbI_2 that uses lead(II) silyamide ($Pb(btsa)_2$) as the lead precursor and tin(IV) iodide (SnI_4) as the iodine precursor was developed recently[89]. As atomic-layer deposition allows precise layer-by-layer control, it has the potential to synthesize molecularly thin 2D perovskites that terminate with a single quantum well.

Interface-confinement method. Colloidal synthesis provides good control of the shape and size of the crystals, but it is challenging to grow large nanosheets using this method. A growth method based on a space-confined aqueous solution, in which the starting solution is confined between two substrates, has been used to achieve large single-crystal perovskites. The method involves injecting the precursor solution between two quartz slides, one prepatterned with a spacer (polyethylene terephthalate) and the other with an electrode (Au) to control the thickness of the growing perovskite. Crystallization occurs under heating[90,91] or upon exposure to the vapour of antisolvent[92] (FIG. 2d). Usually, micrometre-thin single crystals with tuneable lateral sizes ranging from micrometres to millimetres can be obtained. The advantage of this method is that the synthesized crystal has an ultra-smooth surface and can be used directly for device testing.

Alternatively, owing to the restricted translational and rotational symmetry at the water–air interface, this interface can be used to support the self-assembly of monolayers of the organic cation, which can serve as a soft template for the growth of the Pb halide[93]. The surface tension of water induces higher chemical potentials in the precursor molecules, which increases the nucleation probability and accelerates the epitaxial growth of the crystal. RPPs with $n > 1$ have been grown at the water–air interface, where the spontaneous alignment of alkylammonium cations enables uniform orientation and fast in-plane growth. However, the layers grown this way are relatively thick[94]. To date, the direct growth of continuous, molecularly thin RPP films with thicknesses limited to a few unit cells or less remains challenging.

Thickness-dependent optical properties

The optical properties vary with dimensionality (n) across homologous series 2D RPPs. The single-particle bandgap and exciton-binding energies decrease as n increases. The exciton state in $n = 1$ 2D perovskites is delocalized (Wannier type) in the layer and localized (Frenkel type) perpendicular to the layer[18,44,95,96]. As the dimensionality increases, the Frenkel-type exciton becomes more delocalized between the lead-halide layers and eventually transitions to Wannier type at the 3D limit.

The focus in 2D RPPs research has been on how optoelectronic properties change with dimensionality, and much less is known about how the excitonic properties change when the physical thickness is scaled down to the molecularly thin limit. In the limit where the dielectric organic spacers are longer than eight carbon chain lengths, the inorganic layers display effective dielectric and quantum confinements; thus, there seems to be no significant difference in the excitonic properties of a multiple-quantum-well bulk crystal and those of a single-quantum-well monolayer[97]. However, for organic cations with shorter chains, the dielectric environment in a thick perovskite crystal comprising these organic cations differs from that of a single quantum well supported on a substrate. The latter has vacuum on one side and the substrate on the other; thus, the dielectric screening effect is different from that of a bulk crystal surrounded by layers of inorganic lead halides and organic chains[44]. Monolayer semiconductors are particularly sensitive to dielectric screening by the substrate, as was demonstrated in 2D transition-metal dichalcogenides[98–100]; thus, bandgap renormalization may occur for monolayer perovskites on metallic substrates[101].

New phenomena are not restricted to molecularly thin 2D perovskites. There is an intermediate thickness regime in which perovskites have properties distinct from those of the bulk crystal. In particular, the photon recycling effect that is responsible for exciton energy loss is dominant in bulk (>100 nm) crystals,

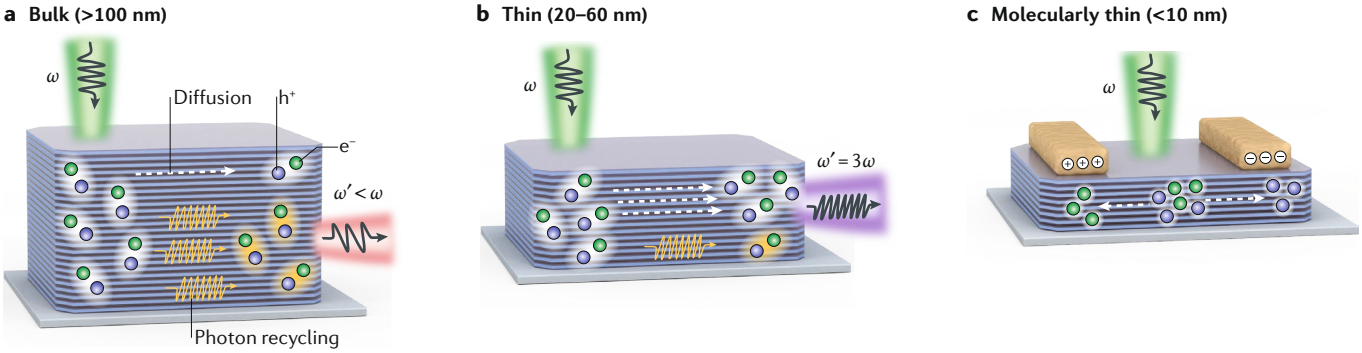

Fig. 3 | **Thickness-dependent optical properties of 2D perovskites. a** | The photon-recycling effect causes fluorescence from the crystal to be reabsorbed as photons travel through the thickness of the crystal, resulting in a red shift of the photoluminescence peak energy. ω, angular frequency. **b** | Non-linear optical effects such as third-harmonic generation are strongest in thin (20–60 nm) 2D perovskite single crystals, in which the photon-recycling effect is suppressed. **c** | Molecularly thin 2D perovskite crystals are the candidate of choice for the fabrication of optoelectronic devices, owing to their ultra-soft nature and good electrical-field permeability.

but is suppressed in thinner crystals (20–60 nm); thus, NLO properties are stronger in the latter (FIG. 3a,b). In terms of electronic-device fabrication, molecularly thin 2D perovskites are the candidate of choice because of their good gate electrostatics and small tunnelling barrier in the vertical direction (FIG. 3c).

Photon recycling. As the thickness of bulk layered perovskites scales down to below 100 nm, there is a gradual blue shift in the absorption and photoluminescence (PL) spectra (FIG. 4a), which should not be confused with shifts due to quantum-confinement effects. Early thickness-dependent optical reflectivity studies on 2D perovskites suggested that the differences in excitonic properties between bulk and exfoliated crystals may come from the structural rearrangement of the organic molecules in the thinner layers[81,102–105]. In fact, the blue shift observed in the optical gap as thickness decreases is best explained by thickness-dependent photon recycling[106–108], a well-known effect in 3D perovskites that is responsible for their excellent performance in solar cells. When photon recycling is present, energy transport is not limited by diffusive-charge transport but can occur over long distances through multiple absorption–diffusion–emission events, leading to red-shifted PL emission spectra (FIG. 3a) and a PL lifetime longer than the intrinsic lifetime[109–112]. A recent study of RPP 2D perovskites confirmed that photon recycling is the major effect contributing to the thickness-dependent PL shift[113]. As a consequence of the strong absorption in 2D perovskites, fluorescence photons propagating through the crystal suffer from a photon reabsorption–emission process over a long propagation distance, resulting in a reduced PL photon energy and intensity as thickness increases[16,114–116]. Conversely, when the crystal thickness is reduced, the photon-recycling effect is suppressed, which gives rise to an apparent blue shift in PL energies. One important outcome of this is the minimization of photon reabsorption at thicknesses below 100 nm, which facilitates stronger NLO effects, as discussed in the next section. A photon-recycling effect between quasi-2D and 3D perovskites in mixed-phase perovskite systems has been invoked to explain the mechanism underlying the good performance of these systems in photovoltaic applications. Besides the rapid diffusion of photocarriers from quasi-2D to 3D regions, the blue-shifted emission originating from the quasi-2D regions is reabsorbed by the 3D perovskite, leading to a boost in photoconductivity associated with longer charge-carrier lifetimes[108].

Phase transitions. Thickness-dependent effects may also influence the phase-transition temperature of perovskite crystals, because the long-range coherence of the crystalline lattice is affected as thickness is reduced and interfacial binding forces exerted by the substrate become increasingly pronounced[117,118]. Although the organic chains have restricted mobility because they are anchored onto the inorganic anion cages, they can, nonetheless, undergo conformational changes that can be coupled to a ferroelectric–paraelectric transition or crystal-phase transition[119]. A high-temperature phase transition can occur, owing to the reorientation of the organic chains adopting a certain packing order, and a low-temperature phase transition can occur, owing to the dynamic disorder of the rigid alkyl moieties[120–126]. Phase transitions driven by organic chains in bulk layered perovskites typically manifest as PL blue shifts with energy in the range of hundreds of meV and at temperatures slightly below room temperature[127]. A study of thin 2D perovskites has shown that the thermally driven structural phase transition is suppressed, and the substrate may play a role[44]. The influence of crystal thickness on phase transitions was revealed by a recent PL study of 2D $(BA)_2PbI_4$, where it was observed that the relative intensities of the emission peaks due to a high-temperature phase (2.39 eV) and a low-temperature phase (2.54 eV) varied with the thickness of the flake. A critical thickness of 25 nm was identified, below which an anomalous change in the phase-transition behaviour occurred due to a surface-depletion electric field that changed the interfacial energy balance between the two phases[128]. More research is needed to understand phase transitions in molecularly thin 2D perovskites, which may be correlated to other effects, such as ferroelectricity.

Disorder and excitonic properties. The softness of molecularly thin 2D perovskites makes them an ideal platform for studying how lattice deformations induced by strain or thermal stress affect the optoelectronic properties. The correlations between dynamic disorder and excitonic properties are known to manifest in various forms, such as defect-induced bound states, polarons and exciton–phonon coupling, all of which have been intensively studied in bulk crystal and polycrystalline films of hybrid perovskites[129–133]. Dynamic disorder is induced by local lattice motion related to the vibrations of the organic cations[134]. As such motions are enhanced in molecularly thin perovskites owing to strain, a stronger dynamic disorder can be expected. Although organic moieties are much lighter than lead atoms, their collective movement can influence internal electric-field distributions, leading to the distortion of the anion cages[135–137]. 2D infrared spectroscopy[138], 2D visible spectroscopy[139] and low-frequency Raman spectra[130] have been used to study the lattice disorder in hybrid perovskites. The ability to generate a reversible order–disorder transition is attractive because it provides a means to engineer the energy landscape in the crystal. Static compression using a high-pressure diamond anvil cell has been used to introduce an order–disorder transition in perovskites, allowing the electronic properties and carrier-recombination lifetime to be tuned[140]; excessive strain ultimately resulted in a disordered energy landscape[141].

Encapsulating single-layer or bilayer RPPs with 2D h-BN generates the equivalent of a diamond micro-anvil. This is because the organic chains are trapped by the h-BN layers and cannot escape, even when irradiated by a laser[40]. This prevents ambient-induced degradation of the perovskites under intense laser irradiation. A reversible PL spectral shift was observed in molecularly thin 2D RPPs under laser irradiation. For a $(BA)_2(MA)Pb_2I_7$ ($n = 2$) RPP, for example, the PL peak shifts from 572 nm to 640 nm under laser irradiation. Interestingly, the PL red shift can be reversed if the sample is subjected to laser annealing under vacuum at a higher irradiance. This reversible spectral shift is attributed to a thermally activated order–disorder transition of the organic–inorganic lattice (FIG. 4b) and can be repeated

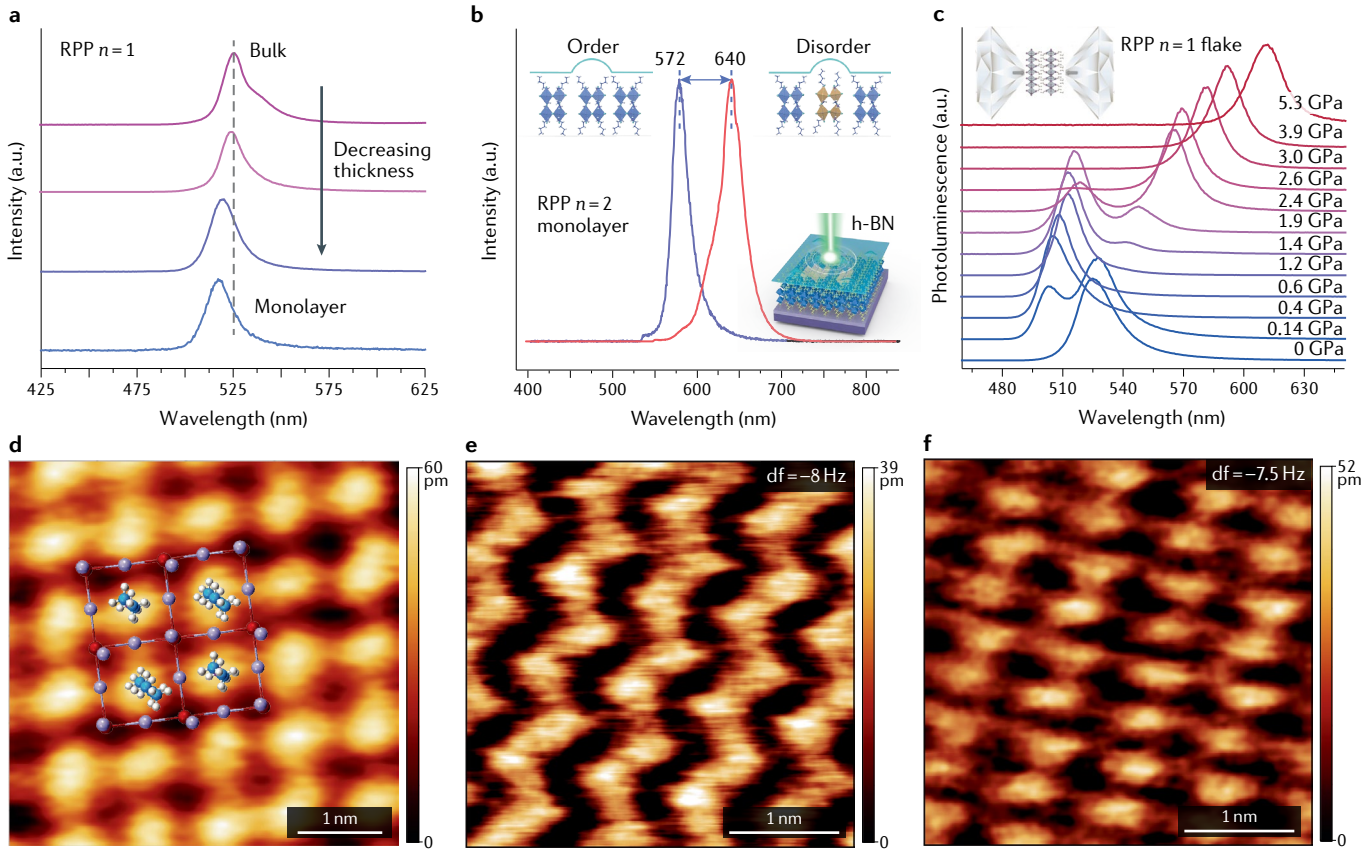

Fig. 4 | **Thickness-dependent and strain-induced changes in photoluminescence energy. a** | As the thickness of a 2D Ruddlesden–Popper perovskite (RPP) decreases from bulk to monolayer (in this case, $(BA)_2PbI_4$; $n = 1$), a blue shift is observed in the photoluminescence (PL) spectra. **b** | Reversible exciton state in a 2D perovskite monolayer encapsulated with hexagonal boron nitride, h-BN (in this case, $(BA)_2(MA)Pb_2I_7$; $n = 2$). Laser illumination activates a reversible order–disorder transition, as demonstrated by the PL shift (the blue curve is the initial state; the red curve is obtained under long laser irradiation; the blue curve can be regenerated if the sample is subjected to a higher-power laser annealing under vacuum). **c** | In situ PL spectra of an exfoliated 2D perovskite flake (50 nm; $(BA)_2PbI_4$; $n = 1$) as a function of pressure in a diamond anvil cell. **d** | Q-plus atomic-force-microscopy image of the surface square lattice of an $n = 4$ RPP flake. The bright dots originate from the organic cations (butylammonium chains), whereas the deep inorganic parts are not imaged. **e**, **f** | Tip-induced reversible surface relaxation (zigzag lattice, panel **e**) and derelaxation (square lattice, panel **f**) of the sample in panel **d**. a.u., arbitrary unit; df, frequency shift. Panels **b** and **d**–**f** adapted from REF.[40], Springer Nature Limited. Panel **c** adapted with permission from REF.[142], ACS.

over tens of cycles, indicating that molecularly thin 2D perovskites encapsulated by h-BN are defect-tolerant. The spectral window of the PL shift is observed to be thickness-dependent, being more pronounced in the monolayer than in thicker layers, which can be explained by the bulk dilution effect, whereby the signal from the surface is masked by the signal from the bulk. Compared with molecularly thin flakes, thicker flakes or bulk crystals of 2D perovskites require a higher pressure to achieve a comparable bandgap narrowing, as revealed by diamond-anvil-cell experiments performed on thick RPP crystals[142,143] (FIG. 4c). For example, a total bandgap narrowing of 350 meV was reported for $(BA)_2PbI_4$ under pressure, which was rationalized by the widening of the Pb–I–Pb bond angle. Moreover, after releasing pressure, the PL emission was recovered to the initial state. Besides bandgap narrowing, a longer exciton lifetime was also observed in the compressed state[144,145].

Visual evidence of the reorientation of the surface organic chains has been captured using a Q-plus non-contact atomic force microscope (AFM), in which the AFM tip served as a local strain source[40]. The surface of as-exfoliated $(BA)_2(MA)_2Pb_4I_{13}$ ($n = 4$) RPP flakes (BA organic chains) exhibits a square lattice (FIG. 4d). By using the AFM tip to apply pressure on the surface, a reversible symmetry transition to a zigzag lattice (FIG. 4e, disordered pattern) from a square lattice (FIG. 4f, ordered pattern) was obtained in the same scan area, reflecting the soft and deformable nature of surface organic cations.

Non-linear optical properties. The realization of efficient and compact all-optical information-processing devices at the nanoscale has attracted great attention in recent years, as they are predicted to overcome the intrinsic speed and heat-dissipation limitations of conventional electronics[146]. Purely non-linear all-optical modulation enables faster operating speed and lower heat generation compared with electro-optical modulation[147]. This strategy uses an initial high-power light pulse (switching beam) that induces NLO effects in the material, such as non-linear absorption and non-linear refraction, to control the propagation of a second low-power pulse (signal). The simplest of these NLO effects is the Kerr effect, which can be described as a change (usually an increase) in the refractive index in proportion to the optical intensity. The refractive index of the medium can be approximated as $\tilde{n} = \tilde{n}_0 + \tilde{n}_2 I$, where $\tilde{n}_0$ is the linear refractive index, $\tilde{n}_2$ is the non-linear refractive index and I is the beam intensity. $\tilde{n}_0$ is usually determined by ellipsometry or absorption measurements, while $\tilde{n}_2$ is traditionally measured by the Z-scan method. 2D RPPs are potential all-optical modulators in the visible and near-infrared range because they exhibit extremely large third-order NLO properties[148]. A material showing a large NLO response can be characterized by its third-order NLO susceptibility, $\chi^{(3)}$, which can be probed by measuring its THG. $\chi^{(3)}$ is a complex material parameter with a real part that is related to the non-linear refractive index, $\tilde{n}_2$ and an imaginary part that is related to the two-photon absorption coefficient, β. Owing to the dielectric and quantum confinement in layered RPP, exciton–exciton interactions under intense optical fields can contribute to a large NLO response[96,149,150]. The breakdown of the translational symmetry in the direction perpendicular to the quantum well ensures rapid radiative decay of 2D excitons and, thus, fast optical-response time of the order of picoseconds or below. Symmetry constraints forbid a second-order non-linear response from centrosymmetric RPP crystals, but third-order non-linear effects, such as the Kerr effect, THG and four-wave mixing, are not bound by these constraints.

Strongly confined quantum structures such as $n = 1$ 2D RPPs are anticipated to exhibit large third-order non-linearity[151,152] as a consequence of their strong excitonic effects. NLO processes, including dipole-forbidden triplet exciton[153], biexciton[154] and triexciton generation[155], THG[152], and four-wave mixing[156,157], have been demonstrated in RPPs. The dependence of $\chi^{(3)}$ on dimensionality in RPPs is not straightforward. According to the Kramers–Kronig two-band model, a dimensionality reduction from $n = 4$ to $n = 1$ results in an increase in bandgap energy, E_g, that should reduce $\tilde{n}_2$ and β according to the inverse power relationships $\tilde{n}^2 \propto E_g^{-4}$ and $\beta \propto E_g^{-3}$ (REFS[158,159]). However, a wavelength-dependent THG and two-photon absorption study on crushed 2D perovskite powder, in which a concomitant increase of bandgap and optical non-linearity was observed, showed that the two-band model does not apply in this case[148]. An unusually large $\tilde{n}_2$ was achieved for an $n = 1$ RPP, despite it having a larger bandgap than its higher homologues, which was explained by efficient quantum confinement in the 2D structure. $\chi^{(3)}$ was measured to be higher than that of the benchmark materials $AgGaSe_2$ and $MAPbI_3$; the latter typically only shows a strong NLO response near resonance[160,161]. Interestingly, the anomalous increase in $\tilde{n}_2$ with increasing bandgap energy was not matched by an increase in β; thus, the interdependence of $\tilde{n}_2$ and β was uncoupled. As a smaller β leads to a lower laser-induced threshold for NLO response[162], the selective enhancement of $\tilde{n}_2$ over β in low-dimensional RPPs is beneficial for high-power and high-efficiency NLO applications.

In addition to dimensionality effects, the physical thickness of RPPs, as well as the presence of grain boundaries, can affect the NLO response. The presence of grain boundaries and defects in polycrystalline samples limits the coherence of 2D excitons, which explains why a stronger NLO signal is typically observed for 2D RPP single crystals. Protecting the surface of 2D RPP single crystals with h-BN enables the study of optical non-linearities in thin flakes without the risk of degradation under laser irradiation. The results reveal that thin RPP flakes in the range 20–60 nm exhibit optimal THG signal[163] (FIG. 5a); this thickness regime has not been studied in the past. The thickness corresponding to the maximum THG signal can be calculated from Maxwell's non-linear equation[164] by accounting for the thickness-dependent absorption of the emitted THG signal, together with the phase-matching conditions between the THG and the fundamental waves. Ultra-strong THG with a maximum effective third-order susceptibility of $1.12 \times 10^{-17}\ m^2\ V^{-2}$ and with a conversion efficiency of 0.006% was observed in $(BA)_2(MA)Pb_2I_7$ flakes. The strong third-order optical response can be

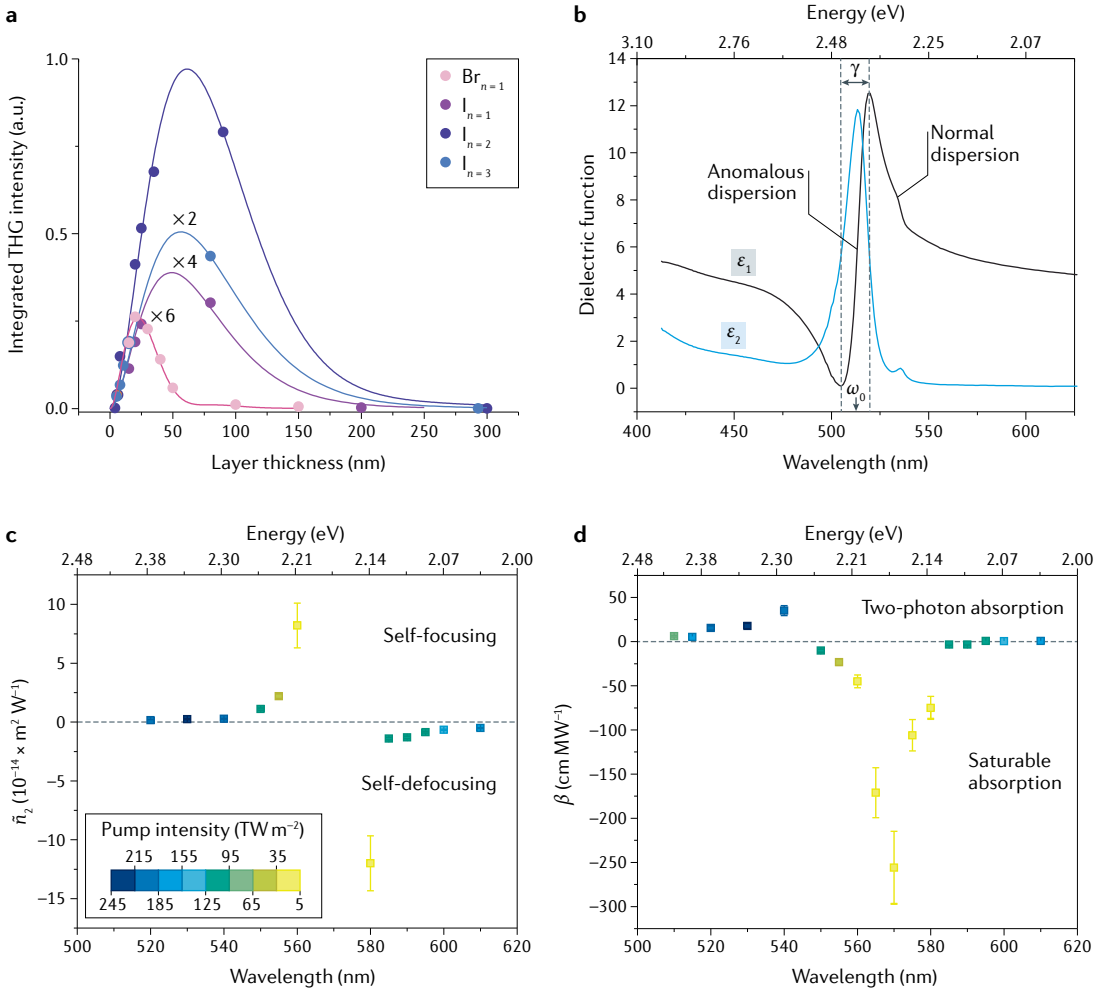

Fig. 5 | **Non-linear optical properties of exfoliated 2D Ruddlesden–Popper perovskite crystals. a** | Third-harmonic generation (THG) signal as a function of layer thickness for four different types of Ruddlesden–Popper perovskite crystals excited at resonance. **b** | The real and imaginary components of the dielectric function of $I_{n=1}$, ε_1 and ε_2, respectively, plotted together for illustration. **c** | Wavelength dependence of the non-linear refractive index, $\tilde{n}_2$, in $I_{n=2}$ at a repetition rate of 1 kHz. The non-linear coefficients are measured with different pump intensities, as indicated by the colour bar. **d** | Two-photon absorption coefficient, β, as a function of wavelength at a repetition rate of 1 kHz for $I_{n=2}$. $Br_{n=1}$: $(C_4H_9NH_3)_2PbBr_4$ ($n=1$); $I_{n=1}$: $(C_4H_9NH_3)_2PbI_4$ ($n=1$); $I_{n=2}$: $(C_4H_9NH_3)_2(CH_3NH_3)Pb_2I_7$ ($n=2$); $I_{n=3}$: $(C_4H_9NH_3)_2(CH_3NH_3)_2Pb_3I_{10}$ ($n=3$); n, number of inorganic metal-halide perovskite layers. Panel **a** adapted with permission from REF.[163], ACS. Panels **b**–**d** adapted with permission from REF.[174], Wiley-VCH.

attributed to a large transition dipole moment boosted by the high exciton-binding energy in the hybrid organic–inorganic multiple quantum wells. The optimal thicknesses for maximum THG signal and the values of the corresponding third-order non-linear susceptibilities for various materials are listed in TABLE 1.

Another interesting possibility is the development of epsilon-near-zero (ENZ) materials[165–169] based on 2D RPPs. ENZ materials exhibit a vanishing real part of the permittivity at a spectral point known as the zero-permittivity wavelength (λ_{ZE}); thus, they provide high conversion efficiencies for harmonic generation when pumped or probed near λ_{ZE}. Degenerately doped semiconductors such as indium tin oxide and gallium-doped ZnO have λ_{ZE} in the near-infrared range[170,171], but they are not CMOS-compatible and have high optical losses. Traditionally, researchers have focused on maximizing $\chi^{(3)}$ to increase $\tilde{n}_2$. Alternatively, the use of ENZ materials, which have a near-zero linear refractive index n_o at λ_{ZE}, allows the non-linear contribution to the refractive index to exceed the linear one, so that $\tilde{n}_2$ becomes anomalously large[167]. Such a situation has been observed in exfoliated RPP $n=1$ single crystals, for which λ_{ZE} is in the visible region. The linear dispersion and absorption properties of the RPP ($n=1$) crystal were investigated using spectroscopic ellipsometry measurements. FIGURE 5b depicts the variation of the real (ε_1) and imaginary (ε_2) components of the complex dielectric function ε, in which ε_1 is related to linear refractive index $\tilde{n}_o$ and ε_2 is related to absorption. Under intense optical pumping near an excitonic resonance, the high oscillator strength of $n=1$ RPP quantum wells generates a large exciton population that provides efficient dipolar screening and phase-space filling, leading to bandgap renormalization and triggering a room-temperature Mott transition to a metal-like ionized plasma[172,173].

Table 1 | **Thicknesses maximizing the third-harmonic generation signal, t_{max}**

Material	t_{max} (nm)	$\chi^{(3)}$ (10^{-18} m^2 V^{-2})	Fundamental wavelength (nm)	Refs
$Br_{n=1}$	22	4.7	1,210	163
$I_{n=1}$	48	3.5	1,500	163
$I_{n=2}$	61	11.2	1,675	163
$I_{n=3}$	56	5.1	1,800	163
Black phosphorous	14.5	0.14	1,557	164
MoS_2	–	0.24	1,560	265
Graphene	–	0.15	1,560	265

$\chi^{(3)}$, third-order non-linear susceptibilities; $Br_{n=1}$, $(C_4H_9NH_3)_2PbBr_4$ ($n=1$); $I_{n=1}$, $(C_4H_9NH_3)_2PbI_4$ ($n=1$); $I_{n=2}$, $(C_4H_9NH_3)_2(CH_3NH_3)Pb_2I_7$ ($n=2$); $I_{n=3}$, $(C_4H_9NH_3)_2(CH_3NH_3)_2Pb_3I_{10}$ ($n=3$); n, number of inorganic metal-halide perovskite layers. No optimal thickness is listed for MoS_2 and graphene because the samples were monolayers. Table adapted with permission from REF.[163], ACS.

This causes ε_1 to approach zero at 506 nm (FIG. 5b). As $\tilde{n}_o$ is related to ε_1, this will cause the refractive index to be dominated by the non-linear index $\tilde{n}_2 I$ ($\tilde{n} = \tilde{n}_o + \tilde{n}_2 I$), thus, giving rise to a giant non-linear response. The Z-scan method is commonly used for measuring the non-linear refractive index (Kerr) coefficient ($\tilde{n}_2$) and non-linear absorption coefficient β. Z-scan measurements as shown in FIG. 5c,d show that the third-order non-linear response $\chi^{(3)}$ of these single crystals can be purely imaginary (when dominated by β with $\tilde{n}_2 = 0$), purely real (when dominated by $\tilde{n}_2$ with $\beta = 0$) or a combination of both (non-zero for both β with $\tilde{n}_2$), depending on the excitation frequency[174]. The magnitude and sign of the non-linear coefficients vary strongly with the excitation wavelength across the excitonic resonance for $n = 2$ RPP, and there is a shift from self-focusing to self-defocusing (FIG. 5c) and from two-photon absorption to saturable absorption for β (FIG. 5d). Two-photon absorption reduces the amount of useful Kerr non-linearity and is a parasitic loss mechanism in optical devices. As β describes two-photon absorption, a zero or low β value means that this loss mechanism is reduced. In fact, a dimensionless figure of merit, $\tilde{n}_2/(\lambda\beta)$, can be used to describe the ratio of Kerr non-linearity to parasitic two-photon absorption. Thus, by selecting the wavelength of light to maximize $\tilde{n}_2$ and minimize β, the figure of merit value can be optimized in RPP. In addition, the strong, saturable-absorber response of RPP crystals at resonance suggests that they are potential candidates for optical modulators for directly generated visible pulsed lasers, which is useful, as there is a lack of efficient optical modulators in the visible region[175,176].

The effective sub-wavelength confinement of light requires the real part of the relative permittivity (ε_1) of the light-trapping medium to be negative. 2D RPPs with low dimensionality ($n = 1$ or 2) can have negative ε_1, owing to their large exciton-binding energy and sizeable oscillator strength. Furthermore, due to the anisotropic excitons of 2D RPPs, they exhibit hyperbolic dispersion (that is, ε_1 has a different sign along orthogonal axes) in the visible range, a feature that was previously observed only in artificial metamaterials[177].

Although 2D RPPs exhibit an exceptionally high and tuneable optical non-linearity near their optical bandgap, off-resonance operation is generally preferred, because pumping or probing the device at the excitonic resonance is disadvantageous, owing to linear absorption, which converts a considerable fraction of light into heat, degrading the modulation performance[178,179]. The resonant and non-resonant all-optical modulation effects in single-crystalline 2D RPP nanosheets ($(BA)_2(MA)Pb_2I_7$ ($n = 2$) and $(BA)_2(MA)_2Pb_4I_{13}$ ($n = 4$) have been investigated using non-degenerate pump–probe spectroscopy with femtosecond pulses. Using sub-bandgap pumping, a 2% reflectivity modulation depth and sub-20-fs temporal response was obtained in the visible and near-infrared spectral regions[180], which would enable modulation speeds of up to >50 THz. The non-resonant ultra-fast behaviour is attributed to a large optical Kerr effect, with two-photon absorption acting as a counteracting effect that prevents an even higher modulation.

Trap states. Trap states play important roles in semiconductor devices by mediating recombination kinetics. The presence of trap states can improve the photoconductive gain of photodetectors by trapping one type of photocarrier (for example, electrons) and suppressing recombination with another type (for example, holes), prolonging the lifetime of photoexcited carriers. The properties of trap states also strongly influence the response or decay time of a photoconductor, because the thermal re-excitation of trapped carriers into the conduction or valence band delays relaxation. Therefore, engineering trap states with the appropriate trapping energies and densities is essential to device performance. The nature of trap states in hybrid perovskites is not well understood, but they are thought to originate from displaced organic cations or halogen vacancies. Iodine interstitial traps, for example, are thought to be relatively benign because of the kinetic deactivation of filled electron traps, which leaves only short-living hole traps[181]. As thinner RPP flakes are more easily deformed by the substrate than thicker flakes, defects may be created at their interfaces, especially on metallic substrates that can have strong ionic interactions with the ammonium ion ends of the organic chains. Lowering the dimensionality of the crystal also results in strong exciton–phonon coupling, thus, giving rise to self-trapped excitons (that is, electron–hole pairs interacting with phonons), which occupy a continuum of sub-gap states below the band edge in the $(BA)_2(MA)_{n-1}Pb_nI_{3n+1}$ series. Such self-trapped states respond to sub-gap excitations, which penetrate deeper into the crystal than above-band-gap excitations to release charge carriers from self-trapped states. By contrast, above-band-gap excitations are strongly absorbed at surfaces, and the photocurrent is suppressed due to surface-charge recombination. The high charge-collection efficiency of these self-trapped excitons was used as the basis for a narrow-bandwidth photodetector, for which a high external quantum efficiency of 200% and a narrow-band photoresponse with a full-width-at-half maximum of less than 60 nm has been reported[182].

Device applications

2D hybrid perovskites have long been in the shadow of 3D hybrid perovskites in the field of photovoltaics. Among the many reasons why 2D perovskites are not the material of choice for photovoltaics is their

high exciton-binding energy, which favours charge recombination over charge separation, although the exciton-binding energies are reduced for the higher-homologue 2D perovskites. The high contact resistance of 2D perovskites, which originates from the insulating organic cations, as well as the tunnelling resistance across multiple organic barriers in the bulk, also obstruct electrical-device applications. One way around the contact problem is to grow vertically oriented quasi-2D perovskites, to the edges of which electrical contacts can be fabricated. This has led to vastly improved power-conversion efficiencies, with solar-cell devices reaching >12% efficiency[28,183]. The main reason for using 2D perovskites, despite the popularity of 3D perovskites, is their relatively high stability. Currently, the power-conversion efficiency of solar cells made from vertically grown, mixed-phase quasi-2D hybrid perovskites exceeds 15%[184]. In this section, we focus on device applications beyond photovoltaics.

Photodetectors. Molecularly thin 2D perovskites are not ideal for photovoltaics, owing to their limited absorption bandwidth. Instead, they are useful as photodetectors. Their molecular-scale thickness allows better gate electrostatics and more efficient carrier extraction compared with bulk perovskites when an electric field is applied. Exfoliated single-crystalline 2D perovskite flakes show thickness-dependent optical contrast on SiO_2/Si substrates and can be manipulated by dry-transfer techniques. However, handling 2D perovskites requires extra care, because their solubility in polar solvents such as water and acetone mean that they are incompatible with conventional lithography techniques. Dry-nanofabrication methods are, thus, required for the fabrication of different 2D perovskite-device architectures. A field-effect transistor (FET) that can be operated both in a lateral and in a vertical configuration has been fabricated in the following way (FIG. 6a): a bottom electrode was first patterned on the substrate (in this case, SiO_2/Si), then, the molecularly thin 2D perovskite was dry transferred on the electrode; with a second dry transfer, a top electrode was placed on the perovskite and, finally, the whole device was encapsulated with h-BN.

Thickness-dependent photoresponsivity has been investigated on $(BA)_2(MA)_2Pb_4I_{13}$ ($n=4$) RPP monocrystalline flakes. The exfoliated flakes were dry transferred onto a two-terminal gold electrode with a 1-μm-long source–drain channel and the device was capped by h-BN to ensure stability[40] (FIG. 6b). The internal quantum efficiency, which is the ratio of the number of charge carriers collected in the photodetector to the number of photons of a given energy absorbed by the detector, was 34%, 44% and 19%, for the monolayer, bilayer and bulk crystal, respectively (FIG. 6c). The higher internal quantum efficiency exhibited by thinner flakes can be rationalized by the greater charge-collection efficiency

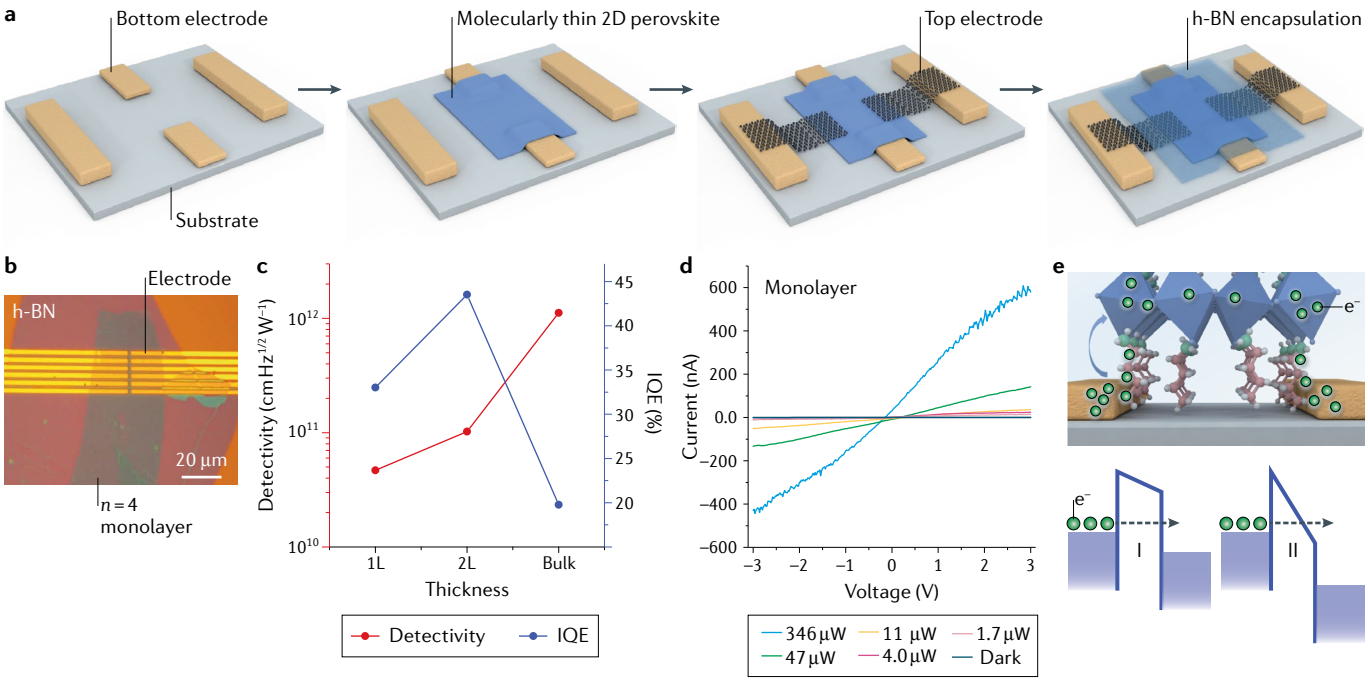

Fig. 6 | **Device fabrication and performance of molecularly thin 2D perovskites. a** | Fabrication of a field-effect transistor. Electrodes (Au) are prepatterned on the substrate (SiO_2/Si) using electron-beam lithography; the 2D perovskite thin flake is then dry transferred on the bottom electrode; graphene is dry transferred on top as the top electrode to obtain a vertical device. Finally, the device is encapsulated with hexagonal boron nitride (h-BN) to ensure its stability. **b** | Optical image of a typical monolayer 2D perovskite device with a bottom Au electrode contact. The source–drain channel width is 1 μm. **c** | Comparison of the internal quantum efficiency (IQE) and detectivity of photodetectors made from monolayer, bilayer and bulk 2D perovskite flakes. The highest IQE values are achieved with molecularly thin samples. **d** | Current versus voltage curves for a monolayer 2D perovskite photodetector under different laser-power densities. The on–off ratio is determined by dividing the light-on current by the dark current. **e** | Schematic diagram of the charge-carrier injection mechanisms at the interface between the organic molecules and the metal electrode: (I) direct tunnelling and (II) Fowler–Nordheim tunnelling. Panels **b–d** adapted from REF.[40], Springer Nature Limited.

of molecularly thin layers as compared with bulk crystals. Due to ultra-low dark current (10^{-13} A), 2D RPP devices exhibit good figures of merit. The calculated photodetectivities increase from 4.7×10^{10} Jones for the monolayer to 1.1×10^{12} Jones for bulk samples under 1 μm² focus laser-spot illumination (FIG. 6c). The photocurrent increases linearly with incident power. At 346 μW incident power, the on/off current ratios are more than 10^5 and 10^6 for monolayer (FIG. 6d) and bulk flakes, respectively. The figures of merit of molecularly thin RPP photodetectors are comparable with those of lateral-structure photodetectors based on organometal-halide 3D perovskites[185].

Recently, self-powered photodetection, in which light is sensed without an external power source, was achieved using $(EA)_2(MA_2)Pb_3Br_{10}$ (EA = ethylammonium), a quasi-2D perovskite showing a stable ferroelectric phase. Ferroelectric photodetector devices separate photocarriers based on ferroelectric polarization, an effect known as bulk photovoltaic effect. The local electrostatic field can reach values of up to 4.2×10^8 V m^{-1}; thus, the dark current is suppressed and a high photoelectric response is obtained. Such ferroelectric photodetectors can exhibit rise and decay times of 96 μs and 123 μs, respectively, and could potentially attain nanosecond responsivity by using a nanosecond laser[186,187].

Field-effect transistors. A detailed understanding of charge transport in perovskites would be important for advancing optoelectronics applications, but is currently elusive. More work needs to be done with regards to the origin of the hysteresis in current–voltage curves, the carrier-scattering mechanism and the effect of ion migration and polaronic effects on transport for both 2D and 3D perovskite crystals. Nonetheless, previous studies on 3D and 2D perovskites provide a reference point for electrical-transport studies on molecularly thin perovskites, such that effects caused solely by thickness changes can be distinguished from a myriad of other effects.

To date, electrical-transport studies have largely been carried out on spin-coated perovskites thin films[188,189] because the fabrication of FETs on thick perovskite single crystals is hampered by electrical-contact issues[190–192]. The carrier-mobility values reported for $MAPbI_3$ range from 100 cm² V^{-1} s^{-1}, measured by contact-free terahertz techniques[193], to much lower mobility values of 1–10 cm² V^{-1} s^{-1} when tested in the FET configuration[194]; the big difference between the two measurement methods originates from contact resistance at the electrode–perovskite interface. Single-crystalline perovskites exhibit higher carrier mobility than their polycrystalline counterparts, but the difference is not large, suggesting that there are other limiting factors besides scattering from grain boundaries and defects. Owing to the ionicity of perovskites, their room-temperature charge-carrier mobilities are fundamentally limited by Fröhlich interactions between charge carriers and the electric fields associated with the longitudinal optical phonon modes of the ionic lattice[195]. However, the overall charge-diffusion length in perovskites is still long because the low carrier mobility is compensated by the long carrier-recombination lifetime[195]. At higher temperatures, charge transport is limited by ion migration, owing to polarization disorder of the MA^+ cations and defects associated with grain boundaries[196].

Two-dimensional semiconductors have attracted attention as channel materials in electronics because of their superior gate electrostatics and ease of integration in miniaturized devices[197]. Therefore, there is interest in scaling down the thickness of 3D perovskites to micrometre or even nanometre dimensions. A method for fabricating a large array of 3D perovskite microplates directly onto prepatterned transistor electrodes was reported[87]: PbI_2 plates were first synthesized on predesigned electrode patterns; then, vapour-phase infusion of methylammonium was used to transform these plates in $CH_3NH_3PbI_3$. Transport studies revealed an electron mobility of 1.0 cm² V^{-1} s^{-1} at 77 K. It is interesting to note that perovskite microplate FETs fabricated on graphene or gold electrodes show different field-effect behaviours. On a gold electrode, the device shows an ambipolar behaviour[198–200], whereas on graphene, a unipolar n-type behaviour was observed[201]. A possible explanation for the n-type behaviour is that, under electrostatic gating, doping of the perovskites by electron transfer from graphene occurs. The field-effect mobility in perovskites decreases with increasing temperature, which is attributed to carrier–phonon scattering and ion migration[198]. Moreover, the hysteresis of the transfer curves increases with temperature. The origins of the hysteresis are not fully understood but have been attributed to a multitude of factors, such as ion migration, surface dipoles, ferroelectricity and trap states[202,203].

FET studies on molecularly thin perovskites are made possible by the availability of mechanically exfoliated flakes of single-crystalline 2D perovskites. Charge-transfer interactions are expected to affect the entire flake, because the length scale is reduced to tens of nanometres. The substrate plays an important role in modulating the electronic properties, similar to what was reported for 2D transition-metal dichalcogenides[98–100]. Owing to the anisotropic properties of 2D perovskites, it can be expected that edge contacts measure a higher charge mobility than vertical contacts, because, when using vertical contacts, charge carriers have to percolate through a van der Waals gap as well as a tunnelling gap on account of the vertically oriented organic chains. A high carrier density of ~10^{21} cm^{-3} has been measured at the edges of exfoliated, ultra-thin 2D perovskites using a conducting AFM, and confocal Raman and PL measurements suggest that these free carriers are not simply due to surface-charge accumulation but originate from non-trivial metallic-edge states[204].

Owing to their highly insulating nature, there are few FET studies on 2D perovskites and existing studies are limited to Sn-based perovskites[205–208], owing to the poor electrical conductivity of Pb-based perovskites[209,210]. The mobility of FETs based on $(PEA)_2SnI_4$ spin-coated films was reported to range from 0.6 to 15 cm² V^{-1} s^{-1} (REFS[211,212]). Compared with Pb-based RPPs, Sn-based RPPs are highly unstable, and self-doping arising from the oxidation of Sn^{2+} to Sn^{4+} reduces charge mobility as a result of scattering from ionized dopant sites[213,214].

Given that the best-performing photovoltaic devices are fabricated using Pb-based perovskites, understanding the charge-transport mechanisms in Pb-based RPPs is important. In particular, $n = 1$ $(BA)_2PbI_4$ perovskites do not have MA^+ cations; thus, charge transport can be studied without the interference of ion migration. Owing to the presence of a top layer of organic chains, the contact between the 2D perovskite layer and metal electrode consists of both a van der Waals gap and a tunnelling gap, similar to the contact in organic transistors[215,216] (FIG. 6e). At the molecularly thin limit, the contact barrier can be approximated by treating the organic chains as resistors. Treated this way, the gap is reminiscent of the tunnelling gap of molecular wires in molecular electronics, where a contact resistance of 0.5–1 eV can be estimated based on the structure of organic cations such as PEA. The charge-carrier-injection mechanism may be quite similar to that of classical organic FETs (FIG. 6e), whereby two distinct transport regimes may be identified, depending on the magnitude of electrical bias applied: direct tunnelling at low bias and Fowler–Nordheim tunnelling at high bias. The magnitude of the injection barrier can be reduced by modifying the π-conjugation and packing of the chains[216].

Ferroelectricity. Low-dimensional semiconducting materials with multiferroic properties are interesting from a fundamental point of view and are potentially attractive for futuristic memory devices that are switchable by multiple levels of control[217,218]. The ferroelectric properties of 2D perovskites have recently come into the spotlight because spontaneous polarization in ferroelectric semiconductors enhances charge separation and can potentially break the Shockley–Queisser limit through the bulk photovoltaic effect[219–223]. A room-temperature ferroelectric phase has been reported in the RPP $((BA)_2(MA)_{(n-1)}Pb_nX_{(3n+1)}$, X = Br or Cl) (REFS[187,224,225]); tuneable ferroelectricity has also been observed in the RPP $(PEA)_2(MA)_{(n-1)}Pb_nI_{(3n+1)}$ and was attributed to correlated reorientation of MA and ion translations[226,227].

The identification of ferroelectricity in 3D hybrid perovskites such as $CH_3NH_3PbI_3$ has been mired in controversy, owing to interfering effects[202,228–231]. Although there have been several papers advocating ferroelectricity in $CH_3NH_3PbI_3$, the observation of hysteresis in the current–voltage sweeps alone cannot be used to prove the presence of ferroelectricity, because hysteresis can also arise from the trapping and detrapping of charges in trap states[203,232]. In addition, the migration of methyl ammonium ions in higher homologues ($n > 1$) can also give rise to hysteresis[233]. The low-temperature orthorhombic phase of $CH_3NH_3PbI_3$ was verified to be centrosymmetric and, thus, not ferroelectric. The dynamic disorder of the methyl ammonium ions makes it difficult to identify the structure of the high-temperature phase. Long-range ferroelectric order is most likely prevented by the dynamic motion of the methyl ammonium ions at room temperature[66]. Detailed studies of the heat capacity and dielectric anomaly across the phase-transition temperature are needed to identify the ferroelectric–paraelectric phase transition.

In perovskite crystals, the ferroelectric–paraelectric phase transition is coupled to a phase change involving the reorientation of organic cations. The static dipole in 2D perovskites comes from the RNH_3^+ organic cations, and the off-centre ordering of RNH_3^+ with respect to the inorganic framework can be coupled to a temperature-dependent phase change that manifests as a ferroelectric–paraelectric transition. $(BA)_2(MA)Pb_2Br_7$ crystals exhibit ferroelectricity with a spontaneous polarization P_s value of ~3.6 μC cm^{-2} (REF.[234]). At room temperature (below $T_c = 352$ K), the crystals adopt a polar structure with MA^+ aligned with the electric polarization along the c-axis direction (ferroelectric phase). When heated to 355 K, they transform to a centrosymmetric structure (paraelectric phase). The anisotropic optical absorption of this polar structure has been explored for polarization-sensitive photodetection in the shortwave region. When excited with polarized light, the resulting device exhibited a high photodetectivity (~10^9 Jones) and fast photoresponse rate (~20 μs).

It is known that a depolarization effect weakens the out-of-plane polarization when thickness is scaled down to the 2D limit[235]. However, owing to the weak van der Waals force coupling between layers, ferroelectricity in 2D perovskites can be sustained down to thicknesses of a few layers[236]. In addition, molecularly thin perovskites require a smaller voltage than bulk films for switching the out-of-plane polarization, while having a higher read-out current. Considering the usually high coercive field required for polarization switching (>0.4 kV cm^{-1}) in bulk 2D perovskites, this makes molecularly thin perovskites attractive for practical operation in memory devices.

One of the basic requirements for ferroelectricity is the absence of centrosymmetry, which can be satisfied by using crystals with a polar space group ($Cmc2_1$), or by breaking surface-inversion symmetry or deforming the inorganic anion cages[227,237]. For example, BA_2PbCl_4 crystallizes into the ferroelectric space group $Cmc2_1$, and the bulk crystal shows a large ferroelectric P_s value of 13 μC cm^{-2} and a high Curie temperature T_c of 438 K (REF.[224]). In-plane ferroelectricity in ultra-thin flakes of BA_2PbCl_4 has been observed at room temperature[238]. The ferroelectricity originates from the displacement of organic cations with respect to the negatively charged $PbCl_6$ octahedra. Taking advantage of the thinness of the exfoliated flakes, a flexible two-terminal electromechanical device was fabricated on the flakes. The device showed piezoelectricity with bending/releasing cycles. The calculated longitudinal piezoelectric coefficient was much higher than that of piezoelectric MoS_2.

Spintronics. The coexistence of strong spin–orbit coupling and ferroelectricity (broken symmetry) in certain lead-halide-based perovskites satisfies the condition for Rashba spin splitting, rendering these perovskites ferroelectric Rashba materials. Rashba splitting arises from the combined effect of spin–orbit interaction and asymmetric crystal potential in the direction perpendicular to the two-dimensional plane, particularly at surfaces or interfaces where the inversion symmetry is broken[239–242]. Dresselhaus splitting applies to cases where the bulk crystal has strong spin–orbit interactions and

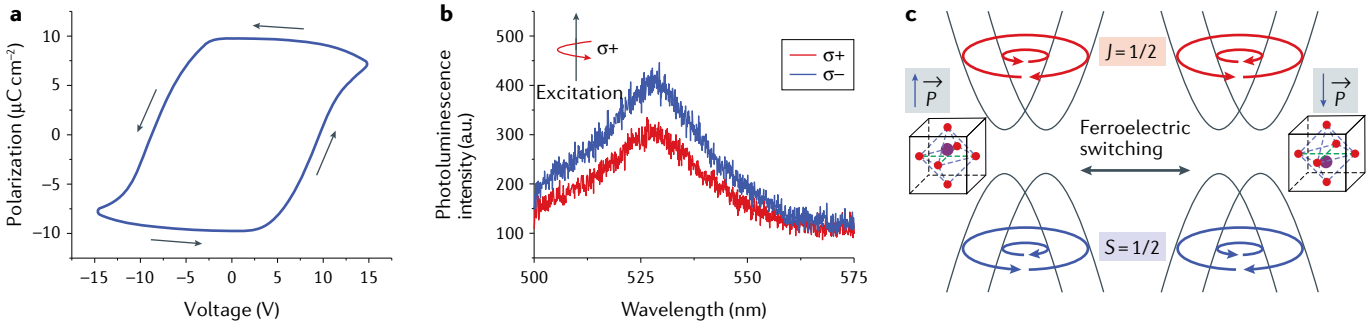

Fig. 7 | **Ferroelectric-coupled Rashba effect in perovskites. a** | Polarization–voltage curve for a Dion–Jacobson hybrid 2D perovskite with the formula of (AMP)PbI_4 (4-(aminomethyl)piperidinium (AMP)), showing a saturated polarization value of 9.8 μC cm^{-2} at room temperature. **b** | Left and right circularly polarized photoluminescence (σ^+ and σ^-, respectively) under left circularly polarized excitation at room temperature for (AMP)PbI_4. The difference in signal for σ^+ and σ^- indicate spin-split bands. **c** | Schematic illustration of the ferroelectric switching of the Rashba effect in a hybrid perovskite. Two types of Rashba bands coexist, one with spin S = ½ at the valence band maximum and one with total angular momentum J = ½ at the conduction band minimum. Their helicity is inverted upon ferroelectric switching. *P*, polarization. Panels **a** and **b** adapted with permission from REF.[243], ACS. Panel **c** adapted with permission from REF.[254], PNAS.

lack inversion symmetry. For example, Dion–Jacobson hybrid perovskites lack centrosymmetry and have Dresselhaus-type spin splitting, whereas other types of bulk-centrosymmetric RPP crystals may have broken inversion symmetry, owing to interface or odd–even parity effects. The presence of Rashba or Dresselhaus splitting gives rise to spin-split bands with opposite optical helicity; thus, under excitation by light of a particular polarization, the intensity of left and right circularly polarized PL will be different. Robust ferroelectricity and spin-split bands have been reported in (AMP)PbI_4 (AMP: 4-(aminomethyl)piperidinium) Dion–Jacobson hybrid perovskites, which displayed a P_s value of 9.8 μC cm^{-2} (FIG. 7a) and a large Rashba splitting energy of 85 meV[243] (FIG. 7b). Ferroelectric polarization switching can lead to new device concepts through the incorporation of ferroic-order parameters in 2D valleytronic systems. In Rashba–Dresselhaus spin splitting, a single parabolic band splits into two spin-polarized bands, which may cause the fundamental bandgap to become indirect; this produces a spin splitting that can couple to the direct or indirect nature of the bandgap[244–246], leading to increased carrier lifetimes and diffusion lengths in hybrid perovskites[247–250]. The Rashba–Dresselhaus effect, thus, provides a means for electronic spin manipulation, which is one of the key requirements for a semiconductor spintronic device[251,252].

The attractiveness of Rashba ferroelectric materials stems from the possibility of coupling ferroelectric polarization to the helical spin texture of the material, thus, affording a means to control spin polarization via electric-field switching[253,254] (FIG. 7c). Most research on hybrid perovskites has focused on verifying the presence of the Rashba effect and quantifying its splitting energy by performing valley-polarized spectroscopy. There has been no experimental demonstration of electrical control of this effect. Rashba splitting parameters in hybrid perovskites are large compared with those observed in conventional III–V semiconductors, making them promising candidates for spintronics[255]. For example, a 160 meV spin splitting in the valence band of single-crystal $CH_3NH_3PbBr_3$ was observed experimentally by angle-resolved photoelectron spectroscopy[256]. A giant Rashba spitting in the 2D perovskite $(C_6H_5C_2H_4NH_3)_2PbI_4$, with a Rashba energy of 40 ± 5 meV, was observed using electro-absorption techniques[257]. Precessional spin relaxation as a consequence of Rashba splitting was observed in $(BA)_2MAPb_2I_7$ using time-resolved circular dichroism[258]. Simulations of the electron spin dynamics yielded a Rashba spin splitting of 10 meV at an electron energy 50 meV above the bandgap, which is 20 times larger than that of GaAs quantum wells[259].

The circular photogalvanic effect has been used to probe the presence and strength of the spin splitting by exciting the sample with circularly polarized light and measuring the helicity-dependent photovoltage or current[260,261]. A helicity-dependent photocurrent was observed in single-crystal $(CH_3NH_3)PbI_3$ (REF.[262]). Spin precession owing to spin–orbit coupling allows the tracking of Rashba-induced spin polarization, as well as of the influence that ferroelectricity has on it.

Compared with bulk crystals or thick films, molecularly thin 2D perovskites are a good host for the Rashba effect, because confinement and symmetry lowering results in richer spin–orbit interactions, and the inversion symmetry can be readily broken by an electrical field or strain. A parity effect has been predicted for Rashba splitting in 2D perovskites, wherein Rashba splitting is anticipated for perovskite crystals with an even number of inorganic layers ($n = 2$), but not for those with an odd number of layers ($n = 1$ and $n = 3$)[250]. Such an odd–even parity effect is predicted for bulk perovskite crystals, but molecularly thin perovskites may show a different behaviour, owing to the lifting of surface-inversion symmetry on account of dynamic disorder induced by strain, electric field or laser irradiation. Owing to the dynamic motion of the methyl ammonium ions, which influences the coupled organic–inorganic degrees of freedom, a dynamic Rashba effect can also occur at elevated temperatures for $n > 1$ perovskites[249].

One advantage of molecularly thin perovskites is that they can serve as tunnelling barrier for charge injectors.

Whereas it is challenging to perform spintronics experiments on thick perovskite crystals owing to their high injection barrier, molecularly thin perovskites have the potential to serve as both tunnelling barrier and spin generator between the charge injector and the spin-carrying material in a Hall-bar device. Taking advantage of their interfacial asymmetry and Rashba effect, charge-to-spin conversion may be possible in 2D perovskites. Alternatively, a charge current injected into a perovskite device can induce a non-equilibrium spin polarization detectable through the inverse spin-galvanic effect.

Outlook

Although bulk hybrid perovskites have been studied for several decades, research on perovskite crystals with thicknesses ranging from monolayer to tens of nanometres is still at a very early stage. The importance of thickness-dependent studies on hybrid perovskites is often overlooked, primarily because researchers are not concerned with the thickness of a single crystallite, and have, so far, relied on spin coating of polycrystalline crystals to control thickness in solar cells and light-emitting diodes. However, in single-crystalline RPP flakes with thickness in the range of 20–60 nm, very strong NLO properties emerge because of phase-matching conditions with the fundamental beam and a suppressed photon-recycling effect. The large third-order susceptibility, combined with a very low linear refractive index near excitonic resonances, can enable an anomalously large Kerr index ($\tilde{n}_2 \approx \chi^{(3)}/n_0$). Precision patterning of 2D perovskites into metasurfaces is expected to lead to a multifold enhancement in their NLO response driven by Fano resonances. Most excitingly, it has been shown that sub-micrometre-thick $n = 1$ RPPs can show ENZ parameters when excited near resonance, where the real part of the permittivity has a crossover from positive to negative values, resulting in insulator-to-metal transition. This means that RPPs can be ENZ materials in the visible part of the electromagnetic spectrum and their NLO properties suggest that they are potential candidates for time-varying media. A 2D perovskite metasurface with a refractive index pulsating at optical frequencies in response to ultra-fast (but spatially uniform) laser pulses would be a remarkable platform for realizing space–time metasurfaces. In space–time metasurfaces, light can experience Doppler-like wavelength shifts, Lorentz non-reciprocity, time-reversed optical behaviour and negative refraction[22,23]. Space–time metasurfaces present the time-reversal features required for a vast number of novel applications, such as magnetic-field-free optical isolators, efficient subwavelength imaging, 'temporal' photonic crystal devices, temporal waveguides, as well as for fundamental quantum field theory studies.

Taking advantage of the fact that molecularly thin perovskites can be mechanically exfoliated from bulk crystal, more research is needed to investigate whether new physics will emerge at the single-quantum-well level. van der Waals heterostructures of 2D perovskites with other 2D materials may be useful for fabricating photodetectors and devices controlled by the proximity effect. For example, a perovskite–MoS_2 heterojunction was reported to exhibit a quantum efficiency of 38%, owing to facile charge separation at the interface between the perovskite and MoS_2 (REF.[263]). Molecularly thin 2D perovskites have a lower series resistance across van der Waals layers than thick crystals; thus, they provide a convenient platform for the fabrication of ferroelectric and spintronic devices. For example, spin-polarized carrier injection from metallic ferromagnetic electrodes into a molecularly thin perovskite could be used to make a spin-polarized light-emitting diode; this has been achieved in 3D perovskites[264]. Spintronic and ferroelectric properties can be combined in 2D perovskites, creating the opportunity for ferroelectric switching of spin orientation and polarization. However, making low-barrier electrical contacts on 2D perovskites is a major bottleneck for realizing devices with high mobility. More research is needed on engineering such low-barrier electrical contacts on 2D perovskites, either by devising schemes to form edge contacts in lateral devices or by selectively removing superficial organic cations. Going beyond mechanical exfoliation, atomic-layer deposition and organic molecular-beam epitaxy might prove useful for large-area growth of molecularly thin 2D perovskites, owing to their precise thickness control. However, further research needs to be performed in this area to bridge the gap between laboratory research and applications.

Published online: 30 March 2020

1. Grancini, G. & Nazeeruddin, M. K. Dimensional tailoring of hybrid perovskites for photovoltaics. *Nat. Rev. Mater.* **4**, 4–22 (2019).
2. Grätzel, M. The rise of highly efficient and stable perovskite solar cells. *Acc. Chem. Res.* **50**, 487–491 (2017).
3. Etgar, L. The merit of perovskite's dimensionality; can this replace the 3D halide perovskite? *Energy Environ. Sci.* **11**, 234–242 (2018).
4. Fu, Y. et al. Metal halide perovskite nanostructures for optoelectronic applications and the study of physical properties. *Nat. Rev. Mater.* **4**, 169–188 (2019).
5. Smith, M. D., Crace, E. J., Jaffe, A. & Karunadasa, H. I. The diversity of layered halide perovskites. *Annu. Rev. Mater. Res.* **48**, 111–136 (2018).
6. Yuan, M. et al. Perovskite energy funnels for efficient light-emitting diodes. *Nat. Nanotechnol.* **11**, 872 (2016).
7. Soe, C. M. M. et al. New type of 2D perovskites with alternating cations in the interlayer space, $(C(NH_2)_3)(CH_3NH_3)_nPb_nI_{3n+1}$: structure, properties, and photovoltaic performance. *J. Am. Chem. Soc.* **139**, 16297–16309 (2017).
8. Saparov, B. & Mitzi, D. B. Organic–inorganic perovskites: structural versatility for functional materials design. *Chem. Rev.* **116**, 4558–4596 (2016).
9. Stoumpos, C. C. et al. Ruddlesden–Popper hybrid lead iodide perovskite 2D homologous semiconductors. *Chem. Mater.* **28**, 2852–2867 (2016).
10. Cao, D. H., Stoumpos, C. C., Farha, O. K., Hupp, J. T. & Kanatzidis, M. G. 2D Homologous perovskites as light-absorbing materials for solar cell applications. *J. Am. Chem. Soc.* **137**, 7843–7850 (2015).
11. Yan, J., Qiu, W., Wu, G., Heremans, P. & Chen, H. Recent progress in 2D/quasi-2D layered metal halide perovskites for solar cells. *J. Mater. Chem. A* **6**, 11063–11077 (2018).
12. Mauck, C. M. & Tisdale, W. A. Excitons in 2D organic–inorganic halide perovskites. *Trends Chem.* **1**, 380–393 (2019).
13. Hong, X., Ishihara, T. & Nurmikko, A. V. Dielectric confinement effect on excitons in PbI_4-based layered semiconductors. *Phys. Rev. B* **45**, 6961–6964 (1992).
14. Tanaka, K. et al. Image charge effect on two-dimensional excitons in an inorganic-organic quantum-well crystal. *Phys. Rev. B* **71**, 045312 (2005).
15. Katan, C., Mercier, N. & Even, J. Quantum and dielectric confinement effects in lower-dimensional hybrid perovskite semiconductors. *Chem. Rev.* **119**, 3140–3192 (2019).
16. Milot, R. L. et al. Charge-carrier dynamics in 2D hybrid metal–halide perovskites. *Nano Lett.* **16**, 7001–7007 (2016).
17. Even, J., Pedesseau, L. & Katan, C. Understanding quantum confinement of charge carriers in layered 2D hybrid perovskites. *ChemPhysChem* **15**, 3733–3741 (2014).
18. Tanaka, K. & Kondo, T. Bandgap and exciton binding energies in lead-iodide-based natural quantum-well crystals. *Sci. Technol. Adv. Mater.* **4**, 599–604 (2003).
19. Tanaka, K. et al. Electronic and excitonic structures of inorganic–organic perovskite-type quantum-well crystal $(C_4H_9NH_3)_2PbBr_4$. *Jpn. J. Appl. Phys.* **44**, 5923–5932 (2005).
20. Kitazawa, N., Aono, M. & Watanabe, Y. Excitons in organic–inorganic hybrid compounds $(C_nH_{2n+1}NH_3)_2PbBr_4$ (n = 4, 5, 7 and 12). *Thin Solid Films* **518**, 3199–3203 (2010).

21. Quan, L. N. et al. Ligand-stabilized reduced-dimensionality perovskites. *J. Am. Chem. Soc.* **138**, 2649–2655 (2016).
22. Smith, I. C., Hoke, E. T., Solis-Ibarra, D., McGehee, M. D. & Karunadasa, H. I. A layered hybrid perovskite solar-cell absorber with enhanced moisture stability. *Angew. Chem. Int. Ed.* **126**, 11414–11417 (2014).
23. Gong, X. et al. Electron–phonon interaction in efficient perovskite blue emitters. *Nat. Mater.* **17**, 550–556 (2018).
24. Du, K.-Z. et al. Two-dimensional lead(II) halide-based hybrid perovskites templated by acene alkylamines: crystal structures, optical properties, and piezoelectricity. *Inorg. Chem.* **56**, 9291–9302 (2017).
25. Hu, T. et al. Mechanism for broadband white-light emission from two-dimensional (110) hybrid perovskites. *J. Phys. Chem. Lett.* **7**, 2258–2263 (2016).
26. Lemmerer, A. & Billing, D. G. Synthesis, characterization and phase transitions of the inorganic–organic layered perovskite-type hybrids $[(C_nH_{2n+1}NH_3)_2PbI_4]$, n = 7, 8, 9 and 10. *Dalton Trans.* **41**, 1146–1157 (2012).
27. Billing, D. G. & Lemmerer, A. Synthesis, characterization and phase transitions of the inorganic–organic layered perovskite-type hybrids $[(C_nH_{2n+1}NH_3)_2PbI_4]$ (n = 12, 14, 16 and 18). *New J. Chem.* **32**, 1736–1746 (2008).
28. Tsai, H. et al. High-efficiency two-dimensional Ruddlesden–Popper perovskite solar cells. *Nature* **536**, 312–316 (2016).
29. Gao, P., Bin Mohd Yusoff, A. R. & Nazeeruddin, M. K. Dimensionality engineering of hybrid halide perovskite light absorbers. *Nat. Commun.* **9**, 5028 (2018).
30. Chen, P. et al. Charge-transfer versus energy-transfer in quasi-2D perovskite light-emitting diodes. *Nano Energy* **50**, 615–622 (2018).
31. Blancon, J.-C. et al. Scaling law for excitons in 2D perovskite quantum wells. *Nat. Commun.* **9**, 2254 (2018).
32. Hintermayr, V. A., Polavarapu, L., Urban, A. S. & Feldmann, J. Accelerated carrier relaxation through reduced coulomb screening in two-dimensional halide perovskite nanoplatelets. *ACS Nano* **12**, 10151–10158 (2018).
33. Xiao, Z., Meng, W., Wang, J., Mitzi, D. B. & Yan, Y. Searching for promising new perovskite-based photovoltaic absorbers: the importance of electronic dimensionality. *Mater. Horiz.* **4**, 206–216 (2017).
34. Chen, Y. et al. 2D Ruddlesden–Popper perovskites for optoelectronics. *Adv. Mater.* **30**, 1703487 (2018).
35. Novoselov, K. S., Mishchenko, A., Carvalho, A. & Castro Neto, A. H. 2D materials and van der Waals heterostructures. *Science* **353**, aac9439 (2016).
36. Novoselov, K. S. et al. Two-dimensional atomic crystals. *Proc. Natl Acad. Sci. USA* **102**, 10451–10453 (2005).
37. Novoselov, K. S. et al. Electric field effect in atomically thin carbon films. *Science* **306**, 666–669 (2004).
38. Ye, Z. et al. Probing excitonic dark states in single-layer tungsten disulphide. *Nature* **513**, 214–218 (2014).
39. Xiao, D., Liu, G.-B., Feng, W., Xu, X. & Yao, W. Coupled spin and valley physics in monolayers of MoS_2 and other group-VI dichalcogenides. *Phys. Rev. Lett.* **108**, 196802 (2012).
40. Leng, K. et al. Molecularly thin two-dimensional hybrid perovskites with tunable optoelectronic properties due to reversible surface relaxation. *Nat. Mater.* **17**, 908–914 (2018).
41. Shi, E. et al. Two-dimensional halide perovskite nanomaterials and heterostructures. *Chem. Soc. Rev.* **47**, 6046–6072 (2018).
42. Dou, L. Emerging two-dimensional halide perovskite nanomaterials. *J. Mater. Chem. C* **5**, 11165–11173 (2017).
43. Miyata, K., Atallah, T. L. & Zhu, X. Y. Lead halide perovskites: Crystal-liquid duality, phonon glass electron crystals, and large polaron formation. *Sci. Adv.* **3**, e1701469 (2017).
44. Yaffe, O. et al. Excitons in ultrathin organic-inorganic perovskite crystals. *Phys. Rev. B* **92**, 045414 (2015).
45. Lippert, S. et al. Influence of the substrate material on the optical properties of tungsten diselenide monolayers. *2D Mater.* **4**, 025045 (2017).
46. Raja, A. et al. Coulomb engineering of the bandgap and excitons in two-dimensional materials. *Nat. Commun.* **8**, 15251 (2017).
47. Reid, O. G., Yang, M., Kopidakis, N., Zhu, K. & Rumbles, G. Grain-size-limited mobility in methylammonium lead iodide perovskite thin films. *ACS Energy Lett.* **1**, 561–565 (2016).
48. Ponseca Jr, C. S. & Sundström, V. Revealing the ultrafast charge carrier dynamics in organo metal halide perovskite solar cell materials using time resolved THz spectroscopy. *Nanoscale* **8**, 6249–6257 (2016).
49. Huang, J., Yuan, Y., Shao, Y. & Yan, Y. Understanding the physical properties of hybrid perovskites for photovoltaic applications. *Nat. Rev. Mater.* **2**, 17042 (2017).
50. Li, Q. et al. Atomic layer dependence of shear modulus in a two-dimensional single-crystal organic–inorganic hybrid perovskite. *J. Phys. Chem. C* **123**, 15251–15257 (2019).
51. Tu, Q. et al. Stretching and breaking of ultrathin 2D hybrid organic–inorganic perovskites. *ACS Nano* **12**, 10347–10354 (2018).
52. Akinwande, D. et al. A review on mechanics and mechanical properties of 2D materials—Graphene and beyond. *Extreme Mech. Lett.* **13**, 42–77 (2017).
53. Sun, S., Fang, Y., Kieslich, G., White, T. J. & Cheetham, A. K. Mechanical properties of organic–inorganic halide perovskites, $CH_3NH_3PbX_3$ (X = I, Br and Cl), by nanoindentation. *J. Mater. Chem. A* **3**, 18450–18455 (2015).
54. Rakita, Y., Cohen, S. R., Kedem, N. K., Hodes, G. & Cahen, D. Mechanical properties of $APbX_3$ (A = Cs or CH_3NH_3; X = I or Br) perovskite single crystals. *MRS Commun.* **5**, 623–629 (2015).
55. Liu, K. et al. Elastic properties of chemical-vapor-deposited monolayer MoS_2, WS_2, and their bilayer heterostructures. *Nano Lett.* **14**, 5097–5103 (2014).
56. Tu, Q. et al. Out-of-plane mechanical properties of 2D hybrid organic–inorganic perovskites by nanoindentation. *ACS Appl. Mater. Interfaces* **10**, 22167–22173 (2018).
57. Bosak, A. et al. Elasticity of hexagonal boron nitride: Inelastic x-ray scattering measurements. *Phys. Rev. B* **73**, 041402 (2006).
58. Jiménez-Riobóo, R. J. et al. In- and out-of-plane longitudinal acoustic-wave velocities and elastic moduli in *h*-BN from Brillouin scattering measurements. *Appl. Phys. Lett.* **112**, 051905 (2018).
59. Blakslee, O. L., Proctor, D. G., Seldin, E. J., Spence, G. B. & Weng, T. Elastic constants of compression-annealed pyrolytic graphite. *J. Appl. Phys.* **41**, 3373–3382 (1970).
60. Seldin, E. J. & Nezbeda, C. W. Elastic constants and electron-microscope observations of neutron-irradiated compression-annealed pyrolytic and single-crystal graphite. *J. Appl. Phys.* **41**, 3389–3400 (1970).
61. Feldman, J. L. Elastic constants of 2H-MoS_2 and 2H-$NbSe_2$ extracted from measured dispersion curves and linear compressibilities. *J. Phys. Chem. Solids* **37**, 1141–1144 (1976).
62. Ji, L.-J. et al. Quantifying the exfoliation ease level of 2D materials via mechanical anisotropy. *Chem. Mater.* **30**, 8732–8738 (2018).
63. Liu, Z. et al. Interlayer binding energy of graphite: a mesoscopic determination from deformation. *Phys. Rev. B* **85**, 205418 (2012).
64. Björkman, T., Gulans, A., Krasheninnikov, A. V. & Nieminen, R. M. van der Waals bonding in layered compounds from advanced density-functional first-principles calculations. *Phys. Rev. Lett.* **108**, 235502 (2012).
65. Wei, T.-C. et al. Photostriction of $CH_3NH_3PbBr_3$ perovskite crystals. *Adv. Mater.* **29**, 1701789 (2017).
66. Zhou, Y. et al. Giant photostriction in organic–inorganic lead halide perovskites. *Nat. Commun.* **7**, 11193 (2016).
67. Chen, B. et al. Large electrostrictive response in lead halide perovskites. *Nat. Mater.* **17**, 1020–1026 (2018).
68. Liu, J. et al. Two-dimensional $CH_3NH_3PbI_3$ perovskite: synthesis and optoelectronic application. *ACS Nano* **10**, 3536–3542 (2016).
69. Ji, D. et al. Freestanding crystalline oxide perovskites down to the monolayer limit. *Nature* **570**, 87–90 (2019).
70. Yang, D. et al. All-inorganic cesium lead halide perovskite nanocrystals: synthesis, surface engineering and applications. *J. Mater. Chem. C* **7**, 757–789 (2019).
71. Dou, L. et al. Atomically thin two-dimensional organic-inorganic hybrid perovskites. *Science* **349**, 1518–1521 (2015).
72. Li, Z. et al. Stabilizing perovskite structures by tuning tolerance factor: formation of formamidinium and cesium lead iodide solid-state alloys. *Chem. Mater.* **28**, 284–292 (2016).
73. Calabrese, J. et al. Preparation and characterization of layered lead halide compounds. *J. Am. Chem. Soc.* **113**, 2328–2330 (1991).
74. Xu, Z., Mitzi, D. B. & Medeiros, D. R. $[(CH_3)_3NCH_2CH_2NH_3]SnI_4$: a layered perovskite with quaternary/primary ammonium dications and short interlayer iodine–iodine contacts. *Inorg. Chem.* **42**, 1400–1402 (2003).
75. Gao, Y. et al. Molecular engineering of organic–inorganic hybrid perovskites quantum wells. *Nat. Chem.* **11**, 1151–1157 (2019).
76. Mao, L., Stoumpos, C. C. & Kanatzidis, M. G. Two-dimensional hybrid halide perovskites: principles and promises. *J. Am. Chem. Soc.* **141**, 1171–1190 (2019).
77. Lanford, O. E. & Kiehl, S. J. The solubility of lead iodide in solutions of potassium iodide-complex lead iodide ions. *J. Am. Chem. Soc.* **63**, 667–669 (1941).
78. Stoumpos, C. C. et al. High members of the 2D Ruddlesden-Popper halide perovskites: synthesis, optical properties, and solar cells of $(CH_3(CH_2)_3NH_3)_2(CH_3NH_3)_4Pb_5I_{16}$. *Chem.* **2**, 427–440 (2017).
79. Wang, J. et al. Controllable growth of centimeter-sized 2D perovskite heterostructures for highly narrow dual-band photodetectors. *ACS Nano* **13**, 5473–5484 (2019).
80. Huang, Y. et al. Reliable exfoliation of large-area high-quality flakes of graphene and other two-dimensional materials. *ACS Nano* **9**, 10612–10620 (2015).
81. Niu, W., Eiden, A., Vijaya Prakash, G. & Baumberg, J. J. Exfoliation of self-assembled 2D organic-inorganic perovskite semiconductors. *Appl. Phys. Lett.* **104**, 171111 (2014).
82. Mao, L. et al. Hybrid Dion–Jacobson 2D lead iodide perovskites. *J. Am. Chem. Soc.* **140**, 3775–3783 (2018).
83. Soe, C. M. M. et al. New type of 2D perovskites with alternating cations in the interlayer space, $(C(NH_2)_3)(CH_3NH_3)_nPb_nI3_{n+1}$: structure, properties, and photovoltaic performance. *J. Am. Chem. Soc.* **139**, 16297–16309 (2017).
84. Kowarik, S., Gerlach, A. & Schreiber, F. Organic molecular beam deposition: fundamentals, growth dynamics, and in situ studies. *J. Phys. Condens. Matter* **20**, 184005 (2008).
85. Li, L. et al. Two-step growth of 2D organic–inorganic perovskite microplates and arrays for functional optoelectronics. *J. Phys. Chem. Lett.* **9**, 4532–4538 (2018).
86. Kitazawa, N., Yaemponga, D., Aono, M. & Watanabe, Y. Optical properties of organic–inorganic hybrid films prepared by the two-step growth process. *J. Lumin.* **129**, 1036–1041 (2009).
87. Wang, G. et al. Wafer-scale growth of large arrays of perovskite microplate crystals for functional electronics and optoelectronics. *Sci. Adv.* **1**, e1500613 (2015).
88. Wang, Y. et al. Chemical vapor deposition growth of single-crystalline cesium lead halide microplatelets and heterostructures for optoelectronic applications. *Nano Res.* **10**, 1223–1233 (2017).
89. Popov, G. et al. Atomic layer deposition of PbI_2 thin films. *Chem. Mater.* **31**, 1101–1109 (2019).
90. Yu, W. et al. Single crystal hybrid perovskite field-effect transistors. *Nat. Commun.* **9**, 5354 (2018).
91. He, X. et al. Oriented growth of ultrathin single crystals of 2D Ruddlesden–Popper hybrid lead iodide perovskites for high-performance photodetectors. *ACS Appl. Mater. Interfaces* **11**, 15905–15912 (2019).
92. Lédée, F. et al. Fast growth of monocrystalline thin films of 2D layered hybrid perovskite. *CrystEngComm* **19**, 2598–2602 (2017).
93. Wang, K., Wu, C., Yang, D., Jiang, Y. & Priya, S. Quasi-two-dimensional halide perovskite single crystal photodetector. *ACS Nano* **12**, 4919–4929 (2018).
94. Zhumekenov, A. A. et al. The role of surface tension in the crystallization of metal halide perovskites. *ACS Energy Lett.* **2**, 1782–1788 (2017).
95. Tanaka, K. et al. Two-dimensional Wannier excitons in a layered-perovskite-type crystal $(C_6H_{13}NH_3)_2PbI_4$. *Solid State Commun.* **122**, 249–252 (2002).
96. Wu, X., Trinh, M. T. & Zhu, X. Y. Excitonic many-body interactions in two-dimensional lead iodide perovskite quantum wells. *J. Phys. Chem. C* **119**, 14714–14721 (2015).
97. Zhang, Q., Chu, L., Zhou, F., Ji, W. & Eda, G. Excitonic properties of chemically synthesized 2D organic–inorganic hybrid perovskite nanosheets. *Adv. Mater.* **30**, 1704055 (2018).
98. Lin, Y. et al. Dielectric screening of excitons and trions in single-layer MoS_2. *Nano Lett.* **14**, 5569–5576 (2014).
99. Ryou, J., Kim, Y.-S., Santosh, K. C. & Cho, K. Monolayer MoS_2 bandgap modulation by dielectric environments and tunable bandgap transistors. *Sci. Rep.* **6**, 29184 (2016).
100. Borghardt, S. et al. Engineering of optical and electronic band gaps in transition metal dichalcogenide monolayers through external dielectric screening. *Phys. Rev. Mater.* **1**, 054001 (2017).

101. Bruix, A. et al. Single-layer MoS_2 on Au(111): band gap renormalization and substrate interaction. *Phys. Rev. B* **93**, 165422 (2016).
102. Pradeesh, K., Baumberg, J. J. & Prakash, G. V. Exciton switching and Peierls transitions in hybrid inorganic-organic self-assembled quantum wells. *Appl. Phys. Lett.* **95**, 173305 (2009).
103. Baranovskii, S. D., Doerr, U., Thomas, P., Naumov, A. & Gebhardt, W. Exciton line broadening by compositional disorder in alloy quantum wells. *Phys. Rev. B* **48**, 17149–17154 (1993).
104. Andreani, L. C., Panzarini, G., Kavokin, A. V. & Vladimirova, M. R. Effect of inhomogeneous broadening on optical properties of excitons in quantum wells. *Phys. Rev. B* **57**, 4670–4680 (1998).
105. Kuznetsova, I. et al. Modeling excitonic line shapes in weakly disordered semiconductor nanostructures. *Phys. Rev. B* **81**, 075307 (2010).
106. Pazos-Outõn, L. M. et al. Photon recycling in lead iodide perovskite solar cells. *Science* **351**, 1430–1433 (2016).
107. Ansari-Rad, M. & Bisquert, J. Insight into photon recycling in perovskite semiconductors from the concept of photon diffusion. *Phys. Rev. Appl.* **10**, 034062 (2018).
108. Motti, S. G. et al. Heterogeneous photon recycling and charge diffusion enhance charge transport in quasi-2D lead-halide perovskite films. *Nano Lett.* **19**, 3953–3960 (2019).
109. Yamada, T., Yamada, Y., Nakaike, Y., Wakamiya, A. & Kanemitsu, Y. Photon emission and reabsorption processes in $CH_3NH_3PbBr_3$ single crystals revealed by time-resolved two-photon-excitation photoluminescence microscopy. *Phys. Rev. Appl.* **7**, 014001 (2017).
110. Diab, H. et al. Impact of reabsorption on the emission spectra and recombination dynamics of hybrid perovskite single crystals. *J. Phys. Chem. Lett.* **8**, 2977–2983 (2017).
111. Miller, O. D., Yablonovitch, E. & Kurtz, S. R. Strong internal and external luminescence as solar cells approach the Shockley–Queisser limit. *IEEE J. Photovolt.* **2**, 303–311 (2012).
112. Zhu, L. et al. Conversion efficiency limits and bandgap designs for multi-junction solar cells with internal radiative efficiencies below unity. *Opt. Express* **24**, A740–A751 (2016).
113. Gan, Z. et al. The dominant energy transport pathway in halide perovskites: photon recycling or carrier diffusion? *Adv. Energy Mater.* **9**, 1900185 (2019).
114. Richter, J. M. et al. Enhancing photoluminescence yields in lead halide perovskites by photon recycling and light out-coupling. *Nat. Commun.* **7**, 13941 (2016).
115. Yamada, Y. et al. Dynamic optical properties of $CH_3NH_3PbI_3$ single crystals as revealed by one- and two-photon excited photoluminescence measurements. *J. Am. Chem. Soc.* **137**, 10456–10459 (2015).
116. Yamada, T. et al. Fast free-carrier diffusion in $CH_3NH_3PbBr_3$ single crystals revealed by time-resolved one- and two-photon excitation photoluminescence spectroscopy. *Adv. Electron. Mater.* **2**, 1500290 (2016).
117. Heinz, H., Vaia, R. A., Krishnamoorti, R. & Farmer, B. L. Self-assembly of alkylammonium chains on montmorillonite: effect of chain length, head group structure, and cation exchange capacity. *Chem. Mater.* **19**, 59–68 (2007).
118. Heinz, H., Castelijns, H. J. & Suter, U. W. Structure and phase transitions of alkyl chains on mica. *J. Am. Chem. Soc.* **125**, 9500–9510 (2003).
119. Abid, H., Trigui, A., Mlayah, A., Hlil, E. K. & Abid, Y. Phase transition in organic–inorganic perovskite $(C_9H_{19}NH_3)_2$ PbI_2Br_2 of long-chain alkylammonium. *Results Phys.* **2**, 71–76 (2012).
120. Salerno, V., Grieco, A. & Vacatello, M. Ordered and disordered phases in mixed dodecylammonium and hexadecylammonium tetrachloromanganate(II). *J. Phys. Chem.* **80**, 2444–2448 (1976).
121. Blinc, R. et al. Proton NMR study of the structural phase transitions in perovskite layer compounds: $(C_nH_{2n+1}NH_3)_2CdCl_4$ and $(NH_3–(CH_2)_n–NH_3)$ $CdCl_4$. *J. Chem. Phys.* **66**, 278–287 (1977).
122. Kind, R. et al. Dynamics of the *n*-decylammonium chains in the perovskite-type layer structure compound $(C_{10}H_{21}NH_3)_2CdCl_4$. *J. Chem. Phys.* **71**, 2118–2130 (1979).
123. Needham, G. F., Willett, R. D. & Franzen, H. F. Phase transitions in crystalline models of bilayers. 1. Differential scanning calorimetric and x-ray studies of $(C_{12}H_{25}NH_3)_2MCl_4$ and $(NH_3C_{14}H_{29}NH_3)_2MCl_4$ salts (M = Mn^{2+}, Cd^{2+}, Cu^{2+}). *J. Phys. Chem.* **88**, 674–680 (1984).
124. Needham, G. F. & Willett, R. D. Phase transitions in crystalline model of lipid bilayer. *J. Phys. Chem.* **85**, 3385–3387 (1981).
125. Casal, H. L., Cameron, D. G. & Mantsch, H. H. Ice melting induced phase transition in diacyl phosphatidylcholines. *J. Phys. Chem.* **87**, 5354–5357 (1983).
126. Almirante, C., Minoni, G. & Zerbi, G. Mechanism of solid to liquidlike phase transition of alkyl chains in bilayer systems. An infrared spectroscopic study of tetradecylammonium tetrachloromanganate $([CH_3(CH_2)_{13}NH_3]_2MnCl_4)$ and tetradecylammonium tetrachlorozincate $[CH_3(CH_2)_{13}NH_3]_2ZnCl_4$. *J. Phys. Chem.* **90**, 852–859 (1986).
127. Ishihara, T., Takahashi, J. & Goto, T. Optical properties due to electronic transitions in two-dimensional semiconductors $(C_nH_{2n+1}NH_3)_2PbI_4$. *Phys. Rev. B* **42**, 11099–11107 (1990).
128. Li, W. et al. Surface depletion field in 2D perovskite microplates: Structural phase transition, quantum confinement and Stark effect. *Nano Res.* **12**, 2858–2865 (2019).
129. Poglitsch, A. & Weber, D. Dynamic disorder in methylammoniumtrihalogenoplumbates (II) observed by millimeter-wave spectroscopy. *J. Chem. Phys.* **87**, 6373–6378 (1987).
130. Yaffe, O. et al. Local polar fluctuations in lead halide perovskite crystals. *Phys. Rev. Lett.* **118**, 136001 (2017).
131. Bakulin, A. A. et al. Real-time observation of organic cation reorientation in methylammonium lead iodide perovskites. *J. Phys. Chem. Lett.* **6**, 3663–3669 (2015).
132. Wu, X. et al. Light-induced picosecond rotational disordering of the inorganic sublattice in hybrid perovskites. *Sci. Adv.* **3**, e1602388 (2017).
133. Miyata, K. et al. Large polarons in lead halide perovskites. *Sci. Adv.* **3**, e1701217 (2017).
134. Even, J., Pedesseau, L. & Katan, C. Analysis of multivalley and multibandgap absorption and enhancement of free carriers related to exciton screening in hybrid perovskites. *J. Phys. Chem. C* **118**, 11566–11572 (2014).
135. Cortecchia, D. et al. Broadband emission in two-dimensional hybrid perovskites: the role of structural deformation. *J. Am. Chem. Soc.* **139**, 39–42 (2017).
136. Smith, M. D., Jaffe, A., Dohner, E. R., Lindenberg, A. M. & Karunadasa, H. I. Structural origins of broadband emission from layered Pb–Br hybrid perovskites. *Chem. Sci.* **8**, 4497–4504 (2017).
137. Cortecchia, D. et al. Polaron self-localization in white-light emitting hybrid perovskites. *J. Mater. Chem. C* **5**, 2771–2780 (2017).
138. Nishida, J. et al. Dynamically disordered lattice in a layered Pb-I-SCN perovskite thin film probed by two-dimensional infrared spectroscopy. *J. Am. Chem. Soc.* **140**, 9882–9890 (2018).
139. Thouin, F. et al. Stable biexcitons in two-dimensional metal-halide perovskites with strong dynamic lattice disorder. *Phys. Rev. Mater.* **2**, 034001 (2018).
140. Zhu, X. Y. & Podzorov, V. Charge carriers in hybrid organic–inorganic lead halide perovskites might be protected as large polarons. *J. Phys. Chem. Lett.* **6**, 4758–4761 (2015).
141. Smith, M. D. & Karunadasa, H. I. White-light emission from layered halide perovskites. *Acc. Chem. Res.* **51**, 619–627 (2018).
142. Yin, T. et al. Pressure-engineered structural and optical properties of two-dimensional $(C_4H_9NH_3)_2PbI_4$ perovskite exfoliated nm-thin flakes. *J. Am. Chem. Soc.* **141**, 1235–1241 (2019).
143. Liu, G. et al. Isothermal pressure-derived metastable states in 2D hybrid perovskites showing enduring bandgap narrowing. *Proc. Natl Acad. Sci. USA* **115**, 8076–8081 (2018).
144. Liu, G. et al. Two regimes of bandgap red shift and partial ambient retention in pressure-treated two-dimensional perovskites. *ACS Energy Lett.* **2**, 2518–2524 (2017).
145. Matsuishi, K., Ishihara, T., Onari, S., Chang, Y. H. & Park, C. H. Optical properties and structural phase transitions of lead-halide based inorganic–organic 3D and 2D perovskite semiconductors under high pressure. *Phys. Status Solidi* **241**, 3328–3333 (2004).
146. Jalali, B. Silicon photonics: Nonlinear optics in the mid-infrared. *Nat. Photonics* **4**, 506–508 (2010).
147. Shcherbakov, M. R. et al. Ultrafast all-optical switching with magnetic resonances in nonlinear dielectric nanostructures. *Nano Lett.* **15**, 6985–6990 (2015).
148. Saouma, F. O., Stoumpos, C. C., Wong, J., Kanatzidis, M. G. & Jang, J. I. Selective enhancement of optical nonlinearity in two-dimensional organic-inorganic lead iodide perovskites. *Nat. Commun.* **8**, 742 (2017).
149. Hanamura, E., Nagaosa, N., Kumagai, M. & Takagahara, T. Quantum wells with enhanced exciton effects and optical non-linearity. *Mater. Sci. Eng. B* **1**, 255–258 (1988).
150. Hanamura, E. Rapid radiative decay and enhanced optical nonlinearity of excitons in a quantum well. *Phys. Rev. B* **38**, 1228–1234 (1988).
151. Wang, J. et al. Giant nonlinear optical response in 2D perovskite heterostructures. *Adv. Opt. Mater.* **7**, 1900398 (2019).
152. Xu, C.-q et al. Optical third-harmonic generation in layered perovskite-type material $(C_{10}H_{21}NH_3)_2PbI_4$. *Solid State Commun.* **79**, 245–248 (1991).
153. Makino, H., Goto, T., Yao, T., Mousdis, G. A. & Papavassiliou, G. C. Induced absorption and spontaneous emission due to biexciton in two-dimensional semiconductor $(CH_3C_6H_4CH_2NH_3)_2PbBr_4$ single crystal. *J. Lumin.* **112**, 54–57 (2005).
154. Kato, Y. et al. Extremely large binding energy of biexcitons in an organic–inorganic quantum-well material $(C_4H_9NH_3)_2PbBr_4$. *Solid State Commun.* **128**, 15–18 (2003).
155. Shimizu, M., Fujisawa, J.-i. & Ishihara, T. Photoluminescence of the inorganic-organic layered semiconductor $(C_6H_5C_2H_4NH_3)_2PbI_4$: Observation of triexciton formation. *Phys. Rev. B* **74**, 155206 (2006).
156. Kondo, T. et al. Resonant third-order optical nonlinearity in the layered perovskite-type material $(C_6H_{13}NH_3)_2PbI_4$. *Solid State Commun.* **105**, 503–506 (1998).
157. Ishi, J., Kunugita, H., Ema, K., Ban, T. & Kondo, T. Influence of exciton-exciton interactions on frequency-mixing signals in a stable exciton-biexciton system. *Phys. Rev. B* **63**, 073303 (2001).
158. Sheik-Bahae, M., Hagan, D. J. & Van Stryland, E. W. Dispersion and band-gap scaling of the electronic Kerr effect in solids associated with two-photon absorption. *Phys. Rev. Lett.* **65**, 96–99 (1990).
159. Sheik-Bahae, M., Hutchings, D. C., Hagan, D. J. & Van Stryland, E. W. Dispersion of bound electron nonlinear refraction in solids. *IEEE J. Quantum Electron.* **27**, 1296–1309 (1991).
160. Zhang, R. et al. Nonlinear optical response of organic–inorganic halide perovskites. *ACS Photonics* **3**, 371–377 (2016).
161. Johnson, J. C., Li, Z., Ndione, P. F. & Zhu, K. Third-order nonlinear optical properties of methylammonium lead halide perovskite films. *J. Mater. Chem. C* **4**, 4847–4852 (2016).
162. Stuart, B. C. et al. Nanosecond-to-femtosecond laser-induced breakdown in dielectrics. *Phys. Rev. B* **53**, 1749–1761 (1996).
163. Abdelwahab, I. et al. Highly enhanced third-harmonic generation in 2D perovskites at excitonic resonances. *ACS Nano* **12**, 644–650 (2018).
164. Youngblood, N., Peng, R., Nemilentsau, A., Low, T. & Li, M. Layer-tunable third-harmonic generation in multilayer black phosphorus. *ACS Photonics* **4**, 8–14 (2017).
165. Reshef, O., De Leon, I., Alam, M. Z. & Boyd, R. W. Nonlinear optical effects in epsilon-near-zero media. *Nat. Rev. Mater.* **4**, 535–551 (2019).
166. Noginov, M. A. et al. Transparent conductive oxides: plasmonic materials for telecom wavelengths. *Appl. Phys. Lett.* **99**, 021101 (2011).
167. Alam, M. Z., De Leon, I. & Boyd, R. W. Large optical nonlinearity of indium tin oxide in its epsilon-near-zero region. *Science* **352**, 795–797 (2016).
168. Luk, T. S. et al. Enhanced third harmonic generation from the epsilon-near-zero modes of ultrathin films. *Appl. Phys. Lett.* **106**, 151103 (2015).
169. Caspani, L. et al. Enhanced nonlinear refractive index in ε-near-zero materials. *Phys. Rev. Lett.* **116**, 233901 (2016).
170. Pradhan, A. K. et al. Extreme tunability in aluminum doped zinc oxide plasmonic materials for near-infrared applications. *Sci. Rep.* **4**, 6415 (2014).
171. Calzolari, A., Ruini, A. & Catellani, A. Transparent conductive oxides as near-IR plasmonic materials: the case of Al-doped ZnO derivatives. *ACS Photonics* **1**, 703–709 (2014).
172. Steinhoff, A. et al. Exciton fission in monolayer transition metal dichalcogenide semiconductors. *Nat. Commun.* **8**, 1166 (2017).
173. Kappei, L., Szczytko, J., Morier-Genoud, F. & Deveaud, B. Direct observation of the Mott transition in an optically excited semiconductor quantum well. *Phys. Rev. Lett.* **94**, 147403 (2005).

174. Abdelwahab, I. et al. Giant and tunable optical nonlinearity in single-crystalline 2D perovskites due to excitonic and plasma effects. *Adv. Mater.* **31**, 1902685 (2019).
175. Gaponenko, M. et al. SESAM mode-locked red praseodymium laser. *Opt. Lett.* **39**, 6939–6941 (2014).
176. Abe, R., Kojou, J., Masuda, K. & Kannari, F. Cr^{4+}-doped $Y_3Al_5O_{12}$ as a saturable absorber for a Q-switched and mode-locked 639-nm Pr^{3+}-doped $LiYF_4$ laser. *Appl. Phys. Express* **6**, 032703 (2013).
177. Guo, P. et al. Hyperbolic dispersion arising from anisotropic excitons in two-dimensional perovskites. *Phys. Rev. Lett.* **121**, 127401 (2018).
178. Cui, Y., Lu, F. & Liu, X. MoS_2-clad microfibre laser delivering conventional, dispersion-managed and dissipative solitons. *Sci. Rep.* **6**, 30524 (2016).
179. Lee, D., Park, K., Debnath, P. C., Kim, I. & Song, Y.-W. Thermal damage suppression of a black phosphorus saturable absorber for high-power operation of pulsed fiber lasers. *Nanotechnology* **27**, 365203 (2016).
180. Grinblat, G. et al. Ultrafast all-optical modulation in 2D hybrid perovskites. *ACS Nano* **13**, 9504–9510 (2019).
181. Meggiolaro, D. et al. Iodine chemistry determines the defect tolerance of lead-halide perovskites. *Energy Environ. Sci.* **11**, 702–713 (2018).
182. Li, J. et al. Self-trapped state enabled filterless narrowband photodetections in 2D layered perovskite single crystals. *Nat. Commun.* **10**, 806 (2019).
183. Blancon, J. C. et al. Extremely efficient internal exciton dissociation through edge states in layered 2D perovskites. *Science* **355**, 1288–1292 (2017).
184. Yang, R. et al. Oriented quasi-2D perovskites for high performance optoelectronic devices. *Adv. Mater.* **30**, 1804771 (2018).
185. Wang, X. et al. Recent progress in organometal halide perovskite photodetectors. *Org. Electron.* **52**, 172–183 (2018).
186. Liu, X. et al. Polarization-driven self-powered photodetection in a single-phase biaxial hybrid perovskite ferroelectric. *Angew. Chem. Int. Ed.* **58**, 14504–14508 (2019).
187. Li, L. et al. Tailored engineering of an unusual $(C_4H_9NH_3)_2(CH_3NH_3)_2Pb_3Br_{10}$ two-dimensional multilayered perovskite ferroelectric for a high-performance photodetector. *Angew. Chem. Int. Ed.* **56**, 12150–12154 (2017).
188. Zeidell, A. M. et al. Enhanced charge transport in hybrid perovskite field-effect transistors via microstructure control. *Adv. Electron. Mater.* **4**, 1800316 (2018).
189. Zhu, L. et al. Synthesis of ultrathin two-dimensional organic–inorganic hybrid perovskite nanosheets for polymer field-effect transistors. *J. Mater. Chem. C* **6**, 3945–3950 (2018).
190. Murali, B. et al. Surface restructuring of hybrid perovskite crystals. *ACS Energy Lett.* **1**, 1119–1126 (2016).
191. Fang, Y., Dong, Q., Shao, Y., Yuan, Y. & Huang, J. Highly narrowband perovskite single-crystal photodetectors enabled by surface-charge recombination. *Nat. Photonics* **9**, 679–686 (2015).
192. Sarmah, S. P. et al. Double charged surface layers in lead halide perovskite crystals. *Nano Lett.* **17**, 2021–2027 (2017).
193. Johnston, M. B. & Herz, L. M. Hybrid perovskites for photovoltaics: charge-carrier recombination, diffusion, and radiative efficiencies. *Acc. Chem. Res.* **49**, 146–154 (2016).
194. Brenner, T. M., Egger, D. A., Kronik, L., Hodes, G. & Cahen, D. Hybrid organic — inorganic perovskites: low-cost semiconductors with intriguing charge-transport properties. *Nat. Rev. Mater.* **1**, 15007 (2016).
195. Herz, L. M. Charge-carrier mobilities in metal halide perovskites: fundamental mechanisms and limits. *ACS Energy Lett.* **2**, 1539–1548 (2017).
196. Senanayak, S. P. et al. Understanding charge transport in lead iodide perovskite thin-film field-effect transistors. *Sci. Adv.* **3**, e1601935 (2017).
197. Liu, Y., Zhang, S., He, J., Wang, Z. M. & Liu, Z. Recent progress in the fabrication, properties, and devices of heterostructures based on 2D materials. *Nanomicro Lett.* **11**, 13 (2019).
198. Chin, X. Y., Cortecchia, D., Yin, J., Bruno, A. & Soci, C. Lead iodide perovskite light-emitting field-effect transistor. *Nat. Commun.* **6**, 7383 (2015).
199. Li, F. et al. Ambipolar solution-processed hybrid perovskite phototransistors. *Nat. Commun.* **6**, 8238 (2015).
200. Mei, Y., Zhang, C., Vardeny, Z. V. & Jurchescu, O. D. Electrostatic gating of hybrid halide perovskite field-effect transistors: balanced ambipolar transport at room-temperature. *MRS Commun.* **5**, 297–301 (2015).
201. Li, D. et al. The effect of thermal annealing on charge transport in organolead halide perovskite microplate field-effect transistors. *Adv. Mater.* **29**, 1601959 (2017).
202. Xiao, Z. et al. Giant switchable photovoltaic effect in organometal trihalide perovskite devices. *Nat. Mater.* **14**, 193–198 (2015).
203. Snaith, H. J. et al. Anomalous hysteresis in perovskite solar cells. *J. Phys. Chem. Lett.* **5**, 1511–1515 (2014).
204. Wang, K. et al. Distinct conducting layer edge states in two-dimensional (2D) halide perovskite. *Sci. Adv.* **5**, eaau3241 (2019).
205. Zhang, F. et al. Two-dimensional organic–inorganic hybrid perovskite field-effect transistors with polymers as bottom-gate dielectrics. *J. Mater. Chem. C* **7**, 4004–4012 (2019).
206. Mitzi, D. B. et al. Hybrid field-effect transistor based on a low-temperature melt-processed channel layer. *Adv. Mater.* **14**, 1772–1776 (2002).
207. Matsushima, T., Fujita, K. & Tsutsui, T. High field-effect hole mobility in organic-inorganic hybrid thin films prepared by vacuum vapor deposition technique. *Jpn. J. Appl. Phys.* **43**, L1199–L1201 (2004).
208. Mitzi, D. B., Dimitrakopoulos, C. D. & Kosbar, L. L. Structurally tailored organic–inorganic perovskites: optical properties and solution-processed channel materials for thin-film transistors. *Chem. Mater.* **13**, 3728–3740 (2001).
209. Noel, N. K. et al. Lead-free organic–inorganic tin halide perovskites for photovoltaic applications. *Energy Environ. Sci.* **7**, 3061–3068 (2014).
210. Hao, F., Stoumpos, C. C., Cao, D. H., Chang, R. P. H. & Kanatzidis, M. G. Lead-free solid-state organic–inorganic halide perovskite solar cells. *Nat. Photonics* **8**, 489–494 (2014).
211. Kagan, C. R., Mitzi, D. B. & Dimitrakopoulos, C. D. Organic-inorganic hybrid materials as semiconducting channels in thin-film field-effect transistors. *Science* **286**, 945–947 (1999).
212. Matsushima, T. et al. Solution-processed organic–inorganic perovskite field-effect transistors with high hole mobilities. *Adv. Mater.* **28**, 10275–10281 (2016).
213. Yang, Z. et al. Stable low-bandgap Pb–Sn binary perovskites for tandem solar cells. *Adv. Mater.* **28**, 8990–8997 (2016).
214. Parrott, E. S. et al. Effect of structural phase transition on charge-carrier lifetimes and defects in $CH_3NH_3SnI_3$ perovskite. *J. Phys. Chem. Lett.* **7**, 1321–1326 (2016).
215. Sirringhaus, H. Device physics of solution-processed organic field-effect transistors. *Adv. Mater.* **17**, 2411–2425 (2005).
216. Liu, C., Xu, Y. & Noh, Y.-Y. Contact engineering in organic field-effect transistors. *Mater. Today* **18**, 79–96 (2015).
217. Wang, H. & Qian, X. Two-dimensional multiferroics in monolayer group IV monochalcogenides. *2D Mater.* **4**, 015042 (2017).
218. Cui, C., Xue, F., Hu, W.-J. & Li, L.-J. Two-dimensional materials with piezoelectric and ferroelectric functionalities. *NPJ 2D Mater. Appl.* **2**, 18 (2018).
219. Paillard, C. et al. Photovoltaics with ferroelectrics: current status and beyond. *Adv. Mater.* **28**, 5153–5168 (2016).
220. Pal, S. et al. Giant photovoltaic response in band engineered ferroelectric perovskite. *Sci. Rep.* **8**, 8005 (2018).
221. Frost, J. M. et al. Atomistic origins of high-performance in hybrid halide perovskite solar cells. *Nano Lett.* **14**, 2584–2590 (2014).
222. Wang, S. et al. An unprecedented biaxial trilayered hybrid perovskite ferroelectric with directionally tunable photovoltaic effects. *J. Am. Chem. Soc.* **141**, 7693–7697 (2019).
223. Spanier, J. E. et al. Power conversion efficiency exceeding the Shockley–Queisser limit in a ferroelectric insulator. *Nat. Photonics* **10**, 611–616 (2016).
224. Liao, W.-Q. et al. A lead-halide perovskite molecular ferroelectric semiconductor. *Nat. Commun.* **6**, 7338 (2015).
225. Li, L. et al. Two-dimensional hybrid perovskite-type ferroelectric for highly polarization-sensitive shortwave photodetection. *J. Am. Chem. Soc.* **141**, 2623–2629 (2019).
226. Zhang, Q. et al. Tunable ferroelectricity in Ruddlesden–Popper halide perovskites. *ACS Appl. Mater. Interfaces* **11**, 13523–13532 (2019).
227. Shi, P.-P. et al. Symmetry breaking in molecular ferroelectrics. *Chem. Soc. Rev.* **45**, 3811–3827 (2016).
228. Kutes, Y. et al. Direct observation of ferroelectric domains in solution-processed $CH_3NH_3PbI_3$ perovskite thin films. *J. Phys. Chem. Lett.* **5**, 3335–3339 (2014).
229. Stroppa, A. et al. Tunable ferroelectric polarization and its interplay with spin–orbit coupling in tin iodide perovskites. *Nat. Commun.* **5**, 5900 (2014).
230. Fan, Z. et al. Ferroelectricity of $CH_3NH_3PbI_3$ perovskite. *J. Phys. Chem. Lett.* **6**, 1155–1161 (2015).
231. Swainson, I. P., Hammond, R. P., Soullière, C., Knop, O. & Massa, W. Phase transitions in the perovskite methylammonium lead bromide, $CH_3ND_3PbBr_3$. *J. Solid State Chem.* **176**, 97–104 (2003).
232. Shao, Y., Xiao, Z., Bi, C., Yuan, Y. & Huang, J. Origin and elimination of photocurrent hysteresis by fullerene passivation in $CH_3NH_3PbI_3$ planar heterojunction solar cells. *Nat. Commun.* **5**, 5784 (2014).
233. Eames, C. et al. Ionic transport in hybrid lead iodide perovskite solar cells. *Nat. Commun.* **6**, 7497 (2015).
234. Li, L. et al. Two-dimensional hybrid perovskite-type ferroelectric for highly polarization-sensitive shortwave photodetection. *J. Am. Chem. Soc.* **141**, 2623–2629 (2019).
235. Junquera, J. & Ghosez, P. Critical thickness for ferroelectricity in perovskite ultrathin films. *Nature* **422**, 506–509 (2003).
236. Liu, F. et al. Room-temperature ferroelectricity in $CuInP_2S_6$ ultrathin flakes. *Nat. Commun.* **7**, 12357 (2016).
237. Sha, T.-T. et al. Fluorinated 2D lead iodide perovskite ferroelectrics. *Adv. Mater.* **31**, 1901843 (2019).
238. You, L. et al. In-plane ferroelectricity in thin flakes of van der Waals hybrid perovskite. *Adv. Mater.* **30**, 1803249 (2018).
239. Rashba, E. Properties of semiconductors with an extremum loop. I. Cyclotron and combinational Resonance in a magnetic field perpendicular to the plane of the loop. *Sov. Phys. Solid State* **2**, 1109–1122 (1960).
240. Dresselhaus, G., Kip, A. F. & Kittel, C. Spin-orbit interaction and the effective masses of holes in germanium. *Phys. Rev.* **95**, 568–569 (1954).
241. Stranks, S. D. & Plochocka, P. The influence of the Rashba effect. *Nat. Mater.* **17**, 381–382 (2018).
242. Ma, J. et al. Chiral 2D perovskites with a high degree of circularly polarized photoluminescence. *ACS Nano* **13**, 3659–3665 (2019).
243. Park, I.-H. et al. Ferroelectricity and Rashba effect in a two-dimensional Dion-Jacobson hybrid organic–inorganic perovskite. *J. Am. Chem. Soc.* **141**, 15972–15976 (2019).
244. Hutter, E. M. et al. Direct–indirect character of the bandgap in methylammonium lead iodide perovskite. *Nat. Mater.* **16**, 115–120 (2017).
245. Zhang, Y. et al. Direct-indirect nature of the bandgap in lead-free perovskite nanocrystals. *J. Phys. Chem. Lett.* **8**, 3173–3177 (2017).
246. Wang, T. et al. Indirect to direct bandgap transition in methylammonium lead halide perovskite. *Energy Environ. Sci.* **10**, 509–515 (2017).
247. Zheng, F., Tan, L. Z., Liu, S. & Rappe, A. M. Rashba spin–orbit coupling enhanced carrier lifetime in $CH_3NH_3PbI_3$. *Nano Lett.* **15**, 7794–7800 (2015).
248. Azarhoosh, P., McKechnie, S., Frost, J. M., Walsh, A. & van Schilfgaarde, M. Research Update: Relativistic origin of slow electron-hole recombination in hybrid halide perovskite solar cells. *APL Mater.* **4**, 091501 (2016).
249. Etienne, T., Mosconi, E. & De Angelis, F. Dynamical origin of the Rashba effect in organohalide lead perovskites: a key to suppressed carrier recombination in perovskite solar cells? *J. Phys. Chem. Lett.* **7**, 1638–1645 (2016).
250. Yin, J. et al. Layer-dependent Rashba band splitting in 2D hybrid perovskites. *Chem. Mater.* **30**, 8538–8545 (2018).
251. Crepaldi, A. et al. Giant ambipolar Rashba effect in the semiconductor BiTeI. *Phys. Rev. Lett.* **109**, 096803 (2012).
252. Maaß, H. et al. Spin-texture inversion in the giant Rashba semiconductor BiTeI. *Nat. Commun.* **7**, 11621 (2016).
253. Kepenekian, M. et al. Rashba and Dresselhaus effects in hybrid organic–inorganic perovskites: from basics to devices. *ACS Nano* **9**, 11557–11567 (2015).
254. Kim, M., Im, J., Freeman, A. J., Ihm, J. & Jin, H. Switchable S = 1/2 and J = 1/2 Rashba bands in

ferroelectric halide perovskites. *Proc. Natl Acad. Sci. USA* **111**, 6900–6904 (2014).
255. Kepenekian, M. & Even, J. Rashba and Dresselhaus couplings in halide perovskites: accomplishments and opportunities for spintronics and spin–orbitronics. *J. Phys. Chem. Lett.* **8**, 3362–3370 (2017).
256. Niesner, D. et al. Giant Rashba splitting in $CH_3NH_3PbBr_3$ organic-inorganic perovskite. *Phys. Rev. Lett.* **117**, 126401 (2016).
257. Zhai, Y. et al. Giant Rashba splitting in 2D organic-inorganic halide perovskites measured by transient spectroscopies. *Sci. Adv.* **3**, e1700704 (2017).
258. Todd, S. B. et al. Detection of Rashba spin splitting in 2D organic-inorganic perovskite via precessional carrier spin relaxation. *APL Mater.* **7**, 081116 (2019).
259. Lau, W. H., Olesberg, J. T. & Flatté, M. E. Electron-spin decoherence in bulk and quantum-well zinc-blende semiconductors. *Phys. Rev. B* **64**, 161301 (2001).
260. Ganichev, S. D. & Golub, L. E. Interplay of Rashba/Dresselhaus spin splittings probed by photogalvanic spectroscopy –A review. *Phys. Status Solidi* **251**, 1801–1823 (2014).
261. Liu, X. et al. Circular photogalvanic spectroscopy of Rashba splitting in 2D hybrid organic–inorganic perovskite multiple quantum wells. *Nat. Commun.* **11**, 323 (2020)
262. Niesner, D. et al. Structural fluctuations cause spin-split states in tetragonal $(CH_3NH_3)PbI_3$ as evidenced by the circular photogalvanic effect. *Proc. Natl Acad. Sci. USA* **115**, 9509–9514 (2018).
263. Fang, C. et al. High-performance photodetectors based on lead-free 2D Ruddlesden–Popper perovskite/MoS_2 heterostructures. *ACS Appl. Mater. Interfaces* **11**, 8419–8427 (2019).
264. Wang, J. et al. Spin-optoelectronic devices based on hybrid organic-inorganic trihalide perovskites. *Nat. Commun.* **10**, 129 (2019).
265. Woodward, R. I. et al. Characterization of the second- and third-order nonlinear optical susceptibilities of monolayer MoS_2 using multiphoton microscopy. *2D Mater.* **4**, 011006 (2017).

Author contributions

K.P.L. and K.L. researched data for the article. All authors discussed the content and contributed to the writing and revising of the manuscript.

Competing interests

The authors declare no competing interests.

Publisher's note

Springer Nature remains neutral with regard to jurisdictional claims in published maps and institutional affiliations.